BNL-205774-2018-JAAM

Mapping canopy defoliation by herbivorous insects at the individual tree level using bi-temporal airborne imaging spectroscopy and LiDAR measurements

R. Meng,

To be published in "Remote Sens. Environ."

June 2018

Environmental and Climate Sciences Department

Brookhaven National Laboratory

U.S. Department of Energy

USDOE Office of Science (SC), Biological and Environmental Research (BER) (SC-23)

Notice: This manuscript has been authored by employees of Brookhaven Science Associates, LLC under Contract No. DE-SC0012704 with the U.S. Department of Energy. The publisher by accepting the manuscript for publication acknowledges that the United States Government retains a non-exclusive, paid-up, irrevocable, world-wide license to publish or reproduce the published form of this manuscript, or allow others to do so, for United States Government purposes.

DISCLAIMER

This report was prepared as an account of work sponsored by an agency of the United States Government. Neither the United States Government nor any agency thereof, nor any of their employees, nor any of their contractors, subcontractors, or their employees, makes any warranty, express or implied, or assumes any legal liability or responsibility for the accuracy, completeness, or any third party's use or the results of such use of any information, apparatus, product, or process disclosed, or represents that its use would not infringe privately owned rights. Reference herein to any specific commercial product, process, or service by trade name, trademark, manufacturer, or otherwise, does not necessarily constitute or imply its endorsement, recommendation, or favoring by the United States Government or any agency thereof or its contractors or subcontractors. The views and opinions of authors expressed herein do not necessarily state or reflect those of the United States Government or any agency thereof.

Mapping canopy defoliation by herbivorous insects at the individual tree level using bi-temporal airborne imaging spectroscopy and LiDAR measurements

Ran Meng[1*], Philip Dennison[2], Feng Zhao[3], Iurii Shendryk[4], Amanda Rickert[1], Ryan Hanavan[5], Bruce Cook[6], and Shawn Serbin[1]

[1] Environmental & Climate Sciences Department, Brookhaven National Laboratory, Upton, New York, NY 11973, USA

[2] Department of Geography, University of Utah, Salt Lake City, UT 84112, USA

[3] Department of Geographical Sciences, University of Maryland, 1165 Lefrak Hall, College Park, MD 20742, USA

[4] CSIRO, Agriculture and Food, St. Lucia, Brisbane, QLD 4067, Australia

[5] USDA Forest Service, Northeastern Area State & Private Forestry, 271 Mast Rd., Durham, NH 03824, USA

[6] Biospheric Sciences Branch, NASA Goddard Space Flight Center, Greenbelt, MD 20742, USA

* Corresponding author: 631-344-3361; ranmeng@bnl.gov

Abstract: Defoliation by herbivorous insects is a widespread forest disturbance driver, affecting global forest health and ecosystem dynamics. Compared with time- and labor-intensive field surveys, remote sensing provides the only realistic approach to mapping canopy defoliation by herbivorous insects over large spatial and temporal scales. However, the spectral and structural signatures of defoliation by insects at the individual tree level have not been well studied. Additionally, the predictive power of spectral and structural metrics for mapping canopy defoliation has seldom been compared. These critical knowledge gaps prevent us from consistently detecting and mapping canopy defoliation by herbivorous insects across multiple scales. During the peak of a gypsy moth outbreak in Long Island, New York in summer 2016, we

leveraged bi-temporal airborne imaging spectroscopy (IS, i.e., hyperspectral imaging) and LiDAR measurements at 1m spatial resolution to explore the spectral and structural signatures of canopy defoliation in a mixed oak-pine forest. We determined that red edge and near-infrared spectral regions within the IS data were most sensitive to crown-scale defoliation severity. LiDAR measurements including B70 (i.e., 70th bincentile height), intensity skewness, and kurtosis were effectively able to detect structural changes caused by herbivorous insects. In addition to canopy leaf loss, increased exposure of understory and non-photosynthetic materials contributed to the detected spectral and structural signatures. Comparing the ability of individual sensors to map canopy defoliation, the LiDAR-only Ordinary Least-Square (OLS) model performed better than the IS-only model (Adj. R-squared = 0.77, RMSE = 15.37% vs. Adj. R-squared = 0.63, RMSE = 19.11%). The IS+LiDAR model improved on performance of the individual sensors (Adj. R-squared = 0.81, RMSE = 14.46%). Our study improves our understanding of spectral and structural signatures of defoliation by herbivorous insects and presents a novel approach for mapping insect defoliation at the individual tree level. Additionally, with the current and next generation of spaceborne sensors (e.g., WorldView-3, Landsat, Sentinel-2, HyspIRI, and GEDI), higher accuracy and frequent monitoring of insect defoliation may become more feasible across a range of spatial scales, which are critical for ecological research and management of forest resources including the economic consequences of forest insect infestations (e.g., reduced growth and increased mortality), as well as for informing and testing of carbon cycle models.

Keywords: Forest infestations, MESMA, invasive species, LiDAR, hyperspectral, data fusion

1. Introduction

Infestation by insects and pathogens is one of most widespread disturbances in forest ecosystems, affecting forest health, ecosystem services, carbon dynamics, and species composition across the globe (Ayres and Lombardero 2000; Kautz et al. 2017a; Kautz et al. 2017b; Seidl et al. 2017; Senf et al. 2017c). In the United States, forest infestation was estimated to be 20 M ha per year, of which 25-50% was attributable to defoliation by herbivorous insects (Dale et al. 2001; Kautz et al. 2017b). The exotic gypsy moth (*Lymantria dispar L.*) is one of the chief defoliators across the northeastern United States. Gypsy moth larvae (caterpillars) feed on leaves of host trees and can defoliate 0.5-1.0 M ha forest per year on average and more than 5.0 M ha in peak years (Elkinton and Liebhold 1990; Man 2010). Also, because the range of gypsy moth is still expanding, studying defoliation by gypsy moth is of high research and management interest (De Beurs and Townsend 2008; Foster et al. 2013; Spruce et al. 2011; Thompson et al. 2017; Townsend et al. 2012).

Insect defoliation does not necessarily result in immediate tree mortality, but can reduce tree growth and trees' resilience to secondary pressures (e.g., drought, wildfire, and hurricanes) (Dale et al. 2001; Gandhi and Herms 2010; Naidoo and Lechowicz 2001). Defoliation can also kill trees after successive defoliation events (Dudley and Bean 2012; Kegg 1971), leading to significant ecological and economic consequences and carbon dynamics (Clark et al. 2010; Coyle et al. 2008; Kenis et al. 2009). Effective detection and monitoring of insect defoliation has thus long been a central focus in the remote sensing, forest ecology and management communities (Coulson et al. 1999; Foster et al. 2013; Landsber and Ohmart 1989; Townsend et al. 2012), and becomes a pressing issue with increasing evidence showing positive interactions

between forest infestation and drier and warmer climate (Kolb et al. 2016; Logan et al. 2003; Seidl et al. 2014; Seidl et al. 2017).

Remote sensing provides the only realistic way for mapping defoliation by herbivorous insects over large spatial and temporal scales (Rullan-Silva et al. 2013; Senf et al. 2017c; Townsend et al. 2012). A wide range of remote sensing data has demonstrated the capacity to monitor spatial-temporal patterns of defoliation by herbivorous insects, including spaceborne multispectral data (e.g., 2m WorldView-2, 10m SPOT, 30m Landsat, and 250m MODIS) (De Beurs and Townsend 2008; Dennison et al. 2009; Franklin et al. 2008; Ji et al. 2017; Meng et al. 2012; Nagler et al. 2014; Oumar and Mutanga 2014; Spruce et al. 2011; Townsend et al. 2012) , airborne imaging spectroscopy (IS, i.e., hyperspectral imaging) data (e.g., 5m HyMap and18m AVIRIS) (Fassnacht et al. 2014; Hanavan et al. 2015; Somers et al. 2010), and airborne Light Detection and Ranging (LiDAR) data (Hanssen and Solberg 2007; Solberg et al. 2006) at multiple spatial scales. Numerous remote sensing-based approaches to mapping defoliation by herbivorous insects have also been developed and applied, such as vegetation indices (Spruce et al. 2011; Townsend et al. 2012), spectral mixture analysis (Radeloff et al. 1999; Somers et al. 2010), and image classification (Kantola et al. 2010; Oumar and Mutanga 2014; Senf et al. 2015).

Vegetation indices applied to 30m Landsat data have been used most widely, e.g., (Hurley et al. 2004; Pasquarella et al. 2017; Townsend et al. 2012), however, these approaches focus solely on broadband spectral responses (i.e., red, near-infrared (NIR), and shortwave near-infrared (SWIR)) to canopy defoliation at >=30m scales. Very high spatial resolution (VHR, <= 5m) multi-spectral sensors, such as GeoEye, QuickBird, and WorldView-2, have been used for mapping and predicting canopy defoliation with relatively higher accuracies, e.g., (Dennison et al. 2010; Oumar and Mutanga 2014; White et al. 2005; Wulder et al. 2008), but most of these studies

91 mainly focused on mapping advanced stages of canopy defoliation (e.g., tree mortality). More
92 importantly, only a few studies have explored the utility of IS or LiDAR for measuring
93 defoliation severity of deciduous broadleaved trees in temperate forest (Hanavan et al. 2015;
94 Hanssen and Solberg 2007; Shendryk et al. 2016; Solberg et al. 2006; Somers et al. 2010).
95 Determination of high resolution spectral and structural signatures of canopy defoliation severity
96 of deciduous broadleaved trees in temperate forest is critical for consistent and precise forest
97 health monitoring at global scale (Millar and Stephenson 2015; Trumbore et al. 2015), but these
98 signatures are still poorly understood. Additionally, few studies have compared the predictive
99 power of spectral and structural metrics and their combination for measuring defoliation severity,
100 and the combined use of spectral and structural metrics has broad implications for the
101 development of next-generation remote sensing frameworks for forest health monitoring (Lausch
102 et al. 2016; White et al. 2016). These critical knowledge gaps need to be filled for consistent and
103 precise detection and mapping of defoliation by herbivorous insects at VHR, which will enable
104 more effective operational forest management (e.g., insect control and fire suppression) and
105 improve our understanding of the effects of insect outbreaks on forest ecology, ecosystem
106 services, and carbon dynamics (Black 2005; Clark et al. 2010; Kenis et al. 2009; Oumar and
107 Mutanga 2014).

108 The development of airborne remote sensing platforms, including VHR optical IS and LiDAR
109 instruments, can help resolve these knowledge gaps (Asner et al. 2017; Cook et al. 2013). By
110 measuring continuous narrowband spectral information, IS data can enhance our ability to
111 remotely assess forest health (Hanavan et al. 2015; Somers et al. 2010). By retrieving detailed
112 three-dimensional information about tree canopies with a high density of laser pulses, LiDAR
113 provides new opportunities for monitoring forest health in the context of the detection and

mapping of forest infestations (Hanssen and Solberg 2007; Shendryk et al. 2016; Solberg et al. 2006). Most prior applications of IS or LiDAR to mapping defoliation by herbivorous insects have focused on pine trees and wood-boring beetles (e.g., mountain pine beetles) (Hanssen and Solberg 2007; Senf et al. 2017c; Solberg et al. 2006), and the potential of combined IS and LiDAR measurements has not been sufficiently assessed and compared for mapping defoliation severity of deciduous broadleaf forests by defoliators like gypsy moth.

Our objective is to explore the crown-scale spectral and structural signatures of canopy defoliation by gypsy moth caterpillars across a defoliation severity gradient and present a novel approach for mapping crown-scale canopy defoliation, which can be easily transferable to other forest ecosystems or forest infestation types. Likely because of consecutive dry springs for the past several years (2014–2016), a severe gypsy moth outbreak occurred and caused widespread canopy defoliation in northeastern United States in early summer 2016 (Pasquarella et al. 2017). During the peak of this defoliation event (i.e., June 14th, 2016), we leveraged the airborne remote sensing platform (i.e., NASA Goddard's LiDAR, Hyperspectral and Thermal (G-LiHT); Cook et al., 2013) to simultaneously measure optical IS and structural LiDAR information at VHR in a mixed oak-pine forest. We chose this study area, because we previously surveyed this area with the airborne G-LiHT platform one year before on an anniversary date (i.e., June 15th, 2015). During ground measurements, we estimated percentage of leaf area remaining, ranging between 0% and 100%, to record defoliation severity at the individual tree level. As defoliation severity is the inverse of percentage of leaf area remaining, 0% leaf area remaining refers to complete canopy defoliation.

Using G-LiHT IS and LiDAR datasets and corresponding ground measurements, we addressed the following research questions: (1) At the crown scale, what are the spectral and structural

signatures of defoliation by herbivorous insects across a defoliation severity gradient? (2) Can biophysical effects (i.e., canopy leaf loss and increased non-photosynthetic material and understory exposure) explain the detected spectral and structural signatures of defoliation by herbivorous insects? (3) What are the differences in predictive power of IS and LiDAR for mapping crown-scale defoliation? (4) Can the combined use of IS and LiDAR improve mapping accuracy?

2. Materials

2.1 Study area

We examined a gypsy moth outbreak event in several mixed oak-pine forest stands located in the Long Island Pine Barrens ecoregion, New York (Fig. 1) during the summer of 2016. The study area has undergone several outbreaks of gypsy moth defoliation for the past three decades. The study area has sandy-flat soils and a moderate-humid climate with evenly-distributed annual precipitation (Kurczewski and Boyle 2000). Annual precipitation is approximately 1,200 mm; annual daily mean temperature is -4.8 C° in January and 21.9 C° in July. Mixed with pitch pine (*Pinus rigida*), the dominant species of broadleaf trees in the study areas are white oak (*Quercus alba L.*), scarlet oak (*Quercus coccinea*), and black oak (*Quercus velutina*). Huckleberry (*Gaylussacia baccata K. Koch*) and blueberry (*Vaccinium spp.)* are the two main shrub species in the study area, which have been found to have an inverse canopy cover relationship with trees (Reiners 1967).

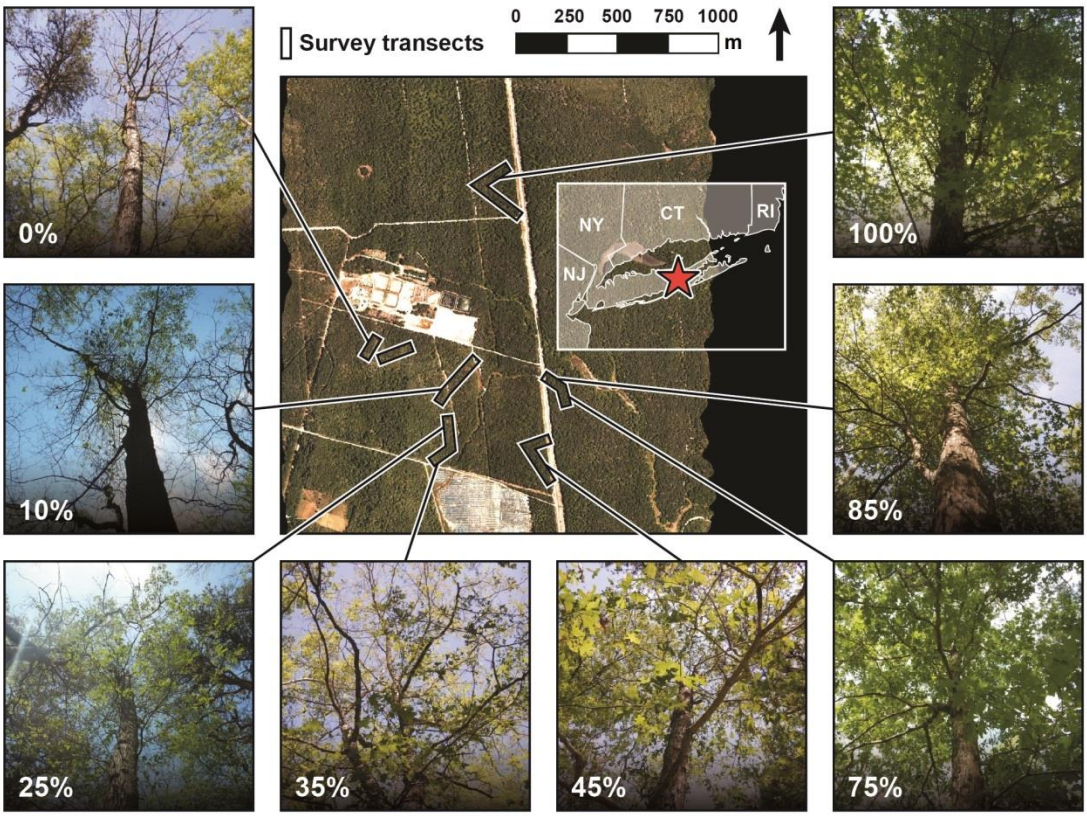

Figure 1. Crown-scale defoliation survey transects within the study area (the background imagery is the true color RGB composition (657 nm (red), 564 nm (green), and 484 nm (blue)) derived from NASA Goddard's LiDAR, Hyperspectral and Thermal (G-LiHT) measurements acquired on June 14, 2016); in-situ pictures showing crown-scale defoliation severity scores (i.e., percentage of leaf area remaining). (For interpretation of the references to color in this figure legend, the reader is referred to the web version of this article.)

2.2 Aerial survey and data preprocessing

We conducted two aerial surveys of the study area (collectively, 800 ha; Fig. 1), with the airborne G-LiHT platform before and during the peak of the gypsy moth outbreak in summer 2015 (i.e., June 15th, 2015) and 2016 (i.e., June 14th, 2016). The bi-temporal aerial surveys were conducted on a sunny day within 2-hour window of local solar noon at a 50° field of view and 200 m average flight altitude. Compared with a single post-disturbance IS and LiDAR dataset, bi-temporal datasets allow measurement of changes in specific tree crowns. G-LiHT

consists of a scanning LiDAR, profiling LiDAR, imaging spectrometer, Global Positioning System and Inertial Navigation System (GPS-INS) and time server, data acquisition computer, and downwelling irradiance spectrometer (Cook et al. 2013). The LiDAR data were collected by an on-board aerial laser scanning (ALS) system (Riegl USA, Orlando, FL, USA) with a mean pulse density of 15-20 laser pulses/m^2. The IS sensor (Headwall Photonics, Fitchburg, MA, USA) collected spectra over the 407–1,007 nm spectral region in 114 spectral bands with a <=5 nm increments (full width half maximum) and a 12-bit radiometric resolution at 1m spatial resolution (Cook et al. 2013). The data used in this study, including at-sensor corrected reflectance (ACR) and georeferenced IS data and coincident LiDAR data at 1m spatial resolution, can be downloaded from the G-LiHT website (http://gliht.gsfc.nasa.gov/).

To ensure consistent temporal reflectance response, we performed radiometric inter-calibrations for the bi-temporal ACR IS imagery. Specifically, we manually selected 3,560 pixels of invariant spectral features (i.e., impervious surfaces) directly on the bi-temporal G-LiHT IS imagery, then we fitted and applied a linear regression model for each IS spectral band, from 2015 against 2016. Inter-calibrated spectra were compared to *in situ* spectra collected on the ground for data quality check (see Section 2.3 below).

2.3 Field measurements

Because defoliation by gypsy moth caterpillars is an ephemeral process, we conducted field measurements of canopy defoliation at the individual tree level within five days of the 2016 G-LiHT aerial survey. Since gypsy moth caterpillars mainly feed on deciduous broadleaf trees (Lippitt et al. 2008), we only measured defoliation status of oak trees within the study area including black oak, scarlet oak, and white oak. To capture a wide variation of canopy

defoliation severity and avoid spatial autocorrelation effects, we established seven variable-length transects ranging between 120 to 250 meter within the study area (Fig. 1). Specifically, we randomly started to sample oak trees from the road edge, and measured every oak tree at least 15 m spatially separated in each transect until reaching the forest interior (Fig. 1).

In total, 91 oak crowns were measured within the study area (Fig. 1). The percentage of leaf area remaining in each survey crown was visually estimated by two technicians separately with 10% intervals, and the two independent estimations were averaged and used as defoliation severity. At the same time, multiple *in-situ* photos were taken for each survey crown for verifying defoliation status afterwards (Fig. 1). Species and diameter at breast height (DBH) were also recorded. Additionally, for checking the quality and potential spectral calibration of G-LiHT IS data, we used a Spectral Evolution PSR+ 3500 spectrometer (http://www.spectralevolution.com/) to collect the ground spectra during the 2016 G-LiHT aerial survey. Specifically, we collected spectra of different land covers on the ground (e.g., soil, grass, concrete road, and litter), ranging between 350-2,500 nm, and each ground sample was measured five times. The center coordinates of all survey tree crowns and field spectra sites were recorded with a hand-held decimeter-level differential global positioning system (dGPS, Trimble Geo7x). After post-processing, the average horizontal accuracy of recorded coordinates was 0.20 m.

3. Methods

To map crown-scale oak canopy defoliation, our workflow was composed of the following steps: (1) LiDAR-based crown segmentation (i.e., individual tree delineation), (2) analysis of spectral and structural signatures of survey crowns, (3) Multiple Endmember Spectral Mixture Analysis (MESMA) applied to IS data in 2015 and 2015, (4) training and comparison of defoliation models, and (5) crown-scale canopy defoliation mapping (Fig. 2).

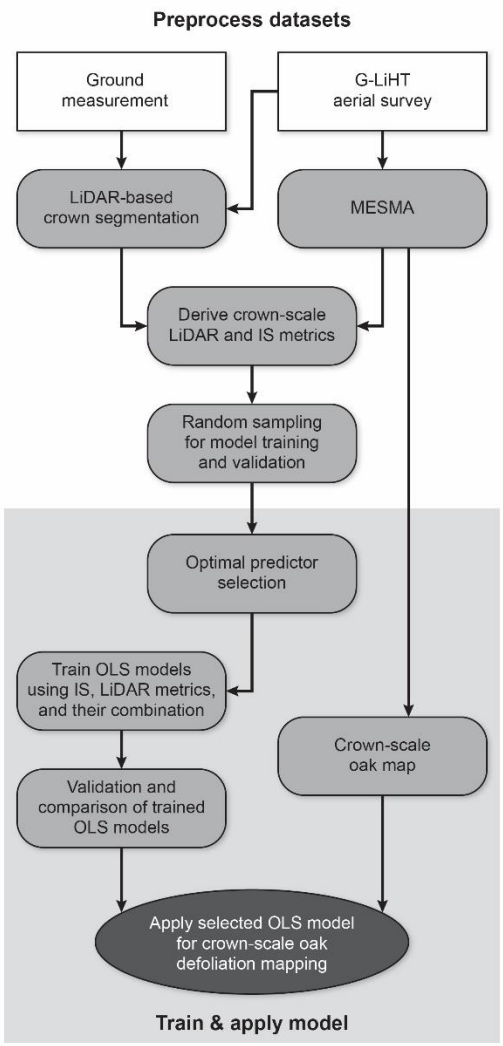

Figure 2. Workflow in this study for mapping canopy defoliation by herbivorous insects at the individual tree level

3.1 LiDAR-based crown segmentation

We applied a top-down segmentation algorithm (Li et al. 2012) to segment tree crowns from the G-LiHT LiDAR point cloud, as the dense understory of Long Island Pine Barrens ecoregion forest limits bottom-up algorithms for detecting individual tree trunks (Lu et al. 2014; Shendryk et al. 2016). This top-down segmentation algorithm isolates trees individually and sequentially from the point cloud, from the tallest tree to the shortest. Starting from a treetop, a target tree is identified by including nearby points and excluding points of other trees based on their horizontal spacing. The main input parameters of the used top-down segmentation algorithm are

1) search radius (R), which is used for identifying local maxima, 2) horizontal threshold (d_{t1}), which is used for including points to a target tree at height lower than 15 m, 3) horizontal threshold (d_{t2}), which is used for including points to a target tree at height higher than 15m, and 4) minimum number of points (n) in a target tree (Li et al. 2012). Based on the 18 forest inventory plot data collected in the same forest area from previous studies (Meng et al., 2017) (see Section 1 in Supplementary materials for more details about the forest inventory data), the following combination of parameters: R of 1.5 m, d_{t1} of 1.5 m; d_{t2} of 3.5 m, and n of 10 points were determined and used to segment tree crowns (see Supplementary materials Section 2 for more details about determining optimal segmentation parameters). The segmentation was performed using Digital Forestry Toolbox (Parkan 2017). We then used the dGPS-recorded coordinates of individual defoliation survey trees to link corresponding polygons of segmented crowns, and used these crown-scale segmentation polygons as the basis for further analysis.

3.2 **Multiple Endmember Spectral Mixture Analysis (MESMA)**

To calculate IS metrics for defoliation mapping and explore the biophysical effects underpinning the spectral and structural signatures of defoliation by gypsy moth caterpillars, we applied MESMA to the G-LiHT IS imagery in 2015 and 2016. MESMA is an expanded version of Linear Spectral Mixture Analysis (LSMA) (Roberts et al. 1998). LSMA decomposes the reflectance of image mixed pixels using a fixed set of spectrally distinct components (i.e., endmembers), enabling the estimations of the relative contribution of a given cover type (i.e., abundance) to pixel reflectance (Drake et al. 1999). MESMA overcomes the LSMA's constraint of modeling all pixels for a given cover type using the same set of endmembers by allowing the endmember model to vary on a pixel-by-pixel basis (Roberts et al. 1998). Specifically, MESMA can use variable endmembers for different endmember models (e.g., two, three, four or more) to

account for within-class spectral variability. Thereby, MESMA can extract biophysical-meaningful information from IS spectra, and has been widely used for remote sensing of forest disturbance studies (Lewis et al. 2017; Meng et al. 2017; Meng et al. 2018; Meng and Zhao 2017; Quintano et al. 2013).

Our application of MESMA consisted of three key steps: spectral library development, selection of optimal endmembers, and modelling. First, we used G-LiHT image spectra to define endmembers for spectral library development. Based on our knowledge of the study area and very high spatial resolution imagery in Google Earth Pro, we manually defined candidate endmembers on the 2016 G-LiHT hyperspectral imagery. Avoiding shadow and edge pixels, we selected about two thousand uniform pixels as candidates for green vegetation (GV) endmembers, including oak, pine, and shrub understory. Endmember Average Root Mean Square Error (EAR; Dennison and Roberts, 2003) was used to select GV endmembers for MESMA. EAR calculates how well each endmember spectrally represents one endmember type. We selected one to two "optimal" endmembers for the following GV types: GV-understory, GV-pine, and GV-oak (Figure 3a). For non-photosynthetic vegetation (NPV) endmembers, we convolved branch and trunk field spectra collected from the study area (Section 2.3) into G-LiHT spectra (Figure 3b). Considering the relatively simple cover types in our study area, we assumed that every G-LiHT IS pixel can be modeled by a three endmember model (i.e. GV-NPV-Shadow). We thus applied a three endmember MESMA model to unmix each G-LiHT IS image.

We set the minimum allowable endmember fraction, maximum allowable endmember fraction, and maximum allowable shade fraction to values of 0.05, 1.05 and 1.0, respectively, and the maximum root-mean-square error (RMSE) to 0.025. All constraint values were based on recommendations for the Visualization and Image Processing for Environmental Research

(VIPER) Tools software package (Roberts et al., 2007), which was used to implement MESMA. MESMA successfully modeled 91.8% of 2015 IS pixels and 94.5% of 2016 IS pixels.

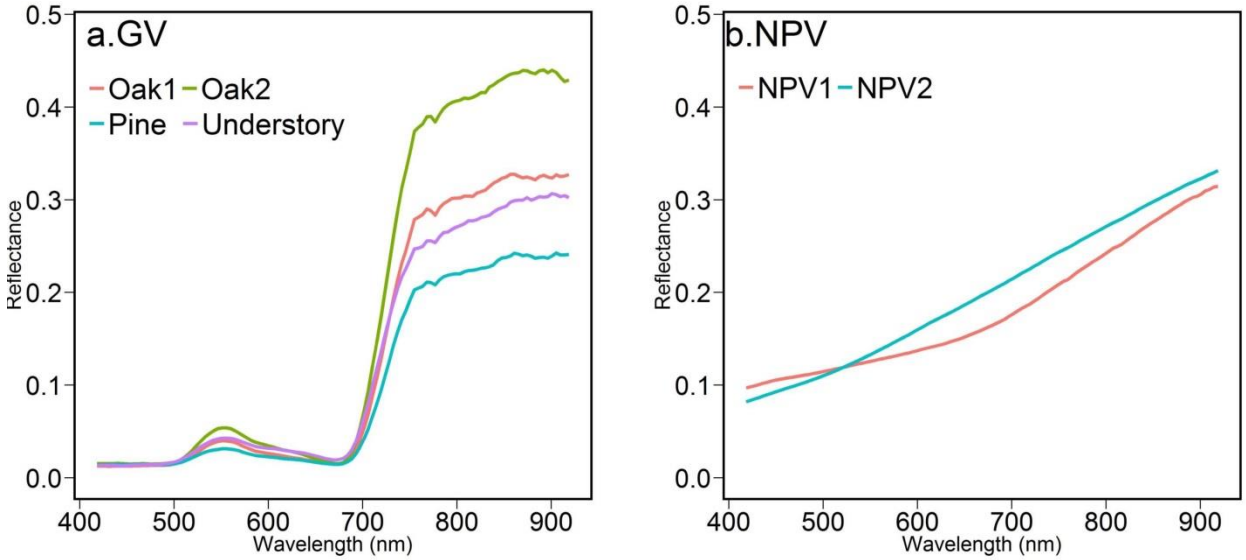

Figure 3. Green vegetation (GV) (a) and non-photosynthetic vegetation (NPV) (b) endmembers selected for use with MESMA. (For interpretation of the references to color in this figure legend, the reader is referred to the web version of this article.)

3.3 LiDAR structural metrics

G-LiHT LiDAR data were used to calculate various structural metrics for mapping defoliation by gypsy moth caterpillars (Table 1). Previous studies have found that LiDAR structural metrics can effectively detect overall structural changes by natural disturbances and thus can be used to assess forest health (Kane et al. 2013; McCarley et al. 2017; Shendryk et al. 2016). We chose these structural metrics, according to their use in other forest disturbance studies (Kane et al. 2013; McCarley et al. 2017; Shendryk et al. 2016). To generate the LiDAR structural metrics, we first binned the bi-temporal G-LiHT LiDAR point clouds into 1-meter voxels. Then all LiDAR structural indices were calculated and converted into individual rasters. We calculated all LiDAR-derived structural metrics using LAStools software suite (https://rapidlasso.com/). Not

274 all structural metrics were finally used, and a variable selection process was applied to select
275 optimal predictors for defoliation modeling (Please see Sections 3.4&3.5 below).

276 **Table 1** Calculated LiDAR-derived structural metrics from 2015 and 2016 G-LiHT aerial data
277 collections used in this study

Index acronym	LiDAR-derive structural metrics	Interpretation
CHM	Canopy height model	Mean vegetation crown height
COV	Canopy cover	Number of first returns above the cover cutoff (i.e., 5m) divided by the number of all first returns and output as a percentage
DNS	Canopy density	Number of all points above the cover cutoff (i.e., 5 m) divided by the number of all returns
QAV	Mean quadratic height	Mean of the quadratic height ($\sum_{i=1}^{n} h_i^2$ /n), h_i is the height of a return point and n is the number of all points)
SKE	Skewness	The skewness of return points
KUR	Kurtosis	The kurtosis of return points
P_{nth}	nth percentile height	nth (i.e., 10, 20, 30, 40, 50, 60, 70, 80, and 90) percentile height value of return points between the ground and the maximum height
Int_ske	Intensity skewness of return intensity	Intensity skewness of return points
Int_kur	Intensity kurtosis of return intensity	Intensity kurtosis of return points
B_{nth}	nth bincentile height	Fraction of return points between the nth (i.e., 10, 20, 30, 40, 50, 60, 70, 80, and 90) percentile height and the maximum height (%)
0-5 m	0-5 m LiDAR return fraction	Fraction of return points in the 0-5m height interval divided by the total number of return points (%)
5-10 m	5-10 m LiDAR return fraction	Fraction of return points within the 5-10m height interval to the total number of return points (%)
10-15 m	10-15 m LiDAR return fraction	Fraction of return points within the 10-15m height interval to the total number of return points (%)
15-20 m	15-20 m LiDAR return fraction	Fraction of return points within the 15-20m height interval to the total number of return points (%)
20-35 m	20-35 m LiDAR return fraction	Fraction of all return points within the 20-35m height interval to the total number of return points (%)

278 **3.4 Comparison of predictive powers for IS, LiDAR and their combination**

279 To train a robust ordinary least squares (OLS) model for mapping crown-scale canopy
280 defoliation, a preliminary screening was first conducted to select optimal predictors from all
281 available predictors derived from G-LiHT IS and LiDAR data. We first calculated mean,
282 minimum, maximum, and standard deviation values for each individual tree crown polygon
283 described in Section 3.1 for 2015 and 2016 MESMA (i.e., oak, pine, understory, and NPV
284 fraction) and structural metrics (Table 1). Then, based on the survey crown dataset, we fit a
285 linear model and calculated Pearson's correlation coefficient (r) for all combinations of 2016
286 predictors and percentage of leaf area remaining at the individual tree level. We also evaluated if
287 univariate models between the response variable and each 2016 predictor variable could be better
288 fit with a second-degree polynomial or logistic regression than with a simple linear relationship,
289 but we did not observe evidence for any other than a linear fit. As such to reduce data
290 redundancy, a threshold of an absolute r value of 0.40 was used to exclude predictors with poor
291 predictive power from further analysis. After the predictor screening, the change in remaining
292 predictors (see Fig. 6 below for a complete list) was calculated (Eq. 1) and used to provide
293 additional predictive variables:

294 $$Change\ in\ Var = Var_{2015} - Var_{2016} \qquad \text{Eq. 1}$$

295 where *Var* is the given variable under study. Then, we performed the following steps for OLS
296 model training and validation: (1) The survey crown dataset was randomly split into training
297 (70%) and validation (30%) dataset. (2) To compare the predictive power of IS, LiDAR, and
298 their combination, the three following options were used for model training: IS: only using IS-
299 derived (i.e., MESMA) variables; LiDAR: only using LiDAR variables; IS+LiDAR: using both
300 IS and LiDAR variables. (3) Using an Akaike Information Criterion (AIC)-based backward
301 method (Burnham and Anderson 2004), we selected important predictors and trained OLS

models for the three options, separately. (4) We applied the three trained OLS models to the validation datasets and assessed their predictive powers using the root mean square error (RMSE; mean Euclidean distance between the prediction in crown-scale oak defoliation and the surveyed oak defoliation) and adjusted R-squared (i.e., the proportion of variability in crown-scale oak defoliation explained by model).

Important variable selection can remove unnecessary predictors and thus reduce collinearity and noise of trained OLS models (Kane et al. 2015; Meng and Dennison 2015). AIC is a metric commonly used to compare the performances of different OLS models (Yamashita et al. 2007). AIC-based backward method starts all available predictors in the OLS model, and then removes the predictor with lowest AIC improvement until all predictors in the OLS model contribute significantly to the OLS model (Yamashita et al. 2007). Remaining uncertainties during the current OLS modeling process include the randomness in splitting between training (70%) and validation (30%) datasets and the potential of over-fitting caused by the relative small size dataset (i.e., 91 crowns). Thereby, we repeated the OLS modeling process one hundred times using randomly selected training and validation data, and then summarized the resulting RMSE and adjusted R-squared results to assess the OLS models.

3.5 Mapping crown-scale oak defoliation

To map canopy defoliation by gypsy moth caterpillars at the individual tree level, we trained an OLS IS+LiDAR model using selected important predictors with a frequency of >=60 (showing best performance, see Section 4.4). To avoid over-fitting, we averaged the coefficient values of IS+LiDAR model from the repeat training results (see Table 2 below) for mapping crown-scale oak defoliation across the study area. An oak crown mask was generated based on the 2015

MESMA results: we classified a crown object as oak if more than 50% pixels within the crown object polygon had >= 0.5 oak endmember fraction value. The accuracy of the oak crown map was assessed using crown-scale oak defoliation and forest inventory field measurements in 2016, and had an overall accuracy of 84% estimated by an error matrix (Table S.1).

The primary assumptions of OLS modeling were also tested and satisfied as below: (1) Normality, by visual analysis of a normal Q-Q plot showing standardized residuals vs. normal scores (Ghasemi and Zahediasl 2012); (2) Co-linearity, by calculations of variance inflation factors (VIF) with a threshold of 10 (O'brien 2007); (3) Homoscedasticity, by visual analysis of a plot showing the standardized residuals vs. the standardized predicted values (Griffith 2009).

4 Results

4.1 Crown-scale spectral signatures of oak defoliation

To avoid noise and show the general trend of oak spectra across a defoliation severity gradient, surveyed oak crowns were grouped into five defoliation severity levels by an equal 20% interval, and the mean spectra of each severity group were calculated and plotted in Fig. 4, consistent with previous similar remote sensing studies (Townsend et al. 2012). In general, the crown-scale oak spectra were sensitive to defoliation severity, with large spectra variations at green, red edge, and NIR wavelengths (Fig. 4). Specifically, red edge slope, associated with vegetative vigor, decreased with defoliation severity; similarly, NIR reflectance, associated with vegetation biomass, also decreased with defoliation severity. Visible reflectance (e.g., green wavelength) did not demonstrate a clear trend with severity.

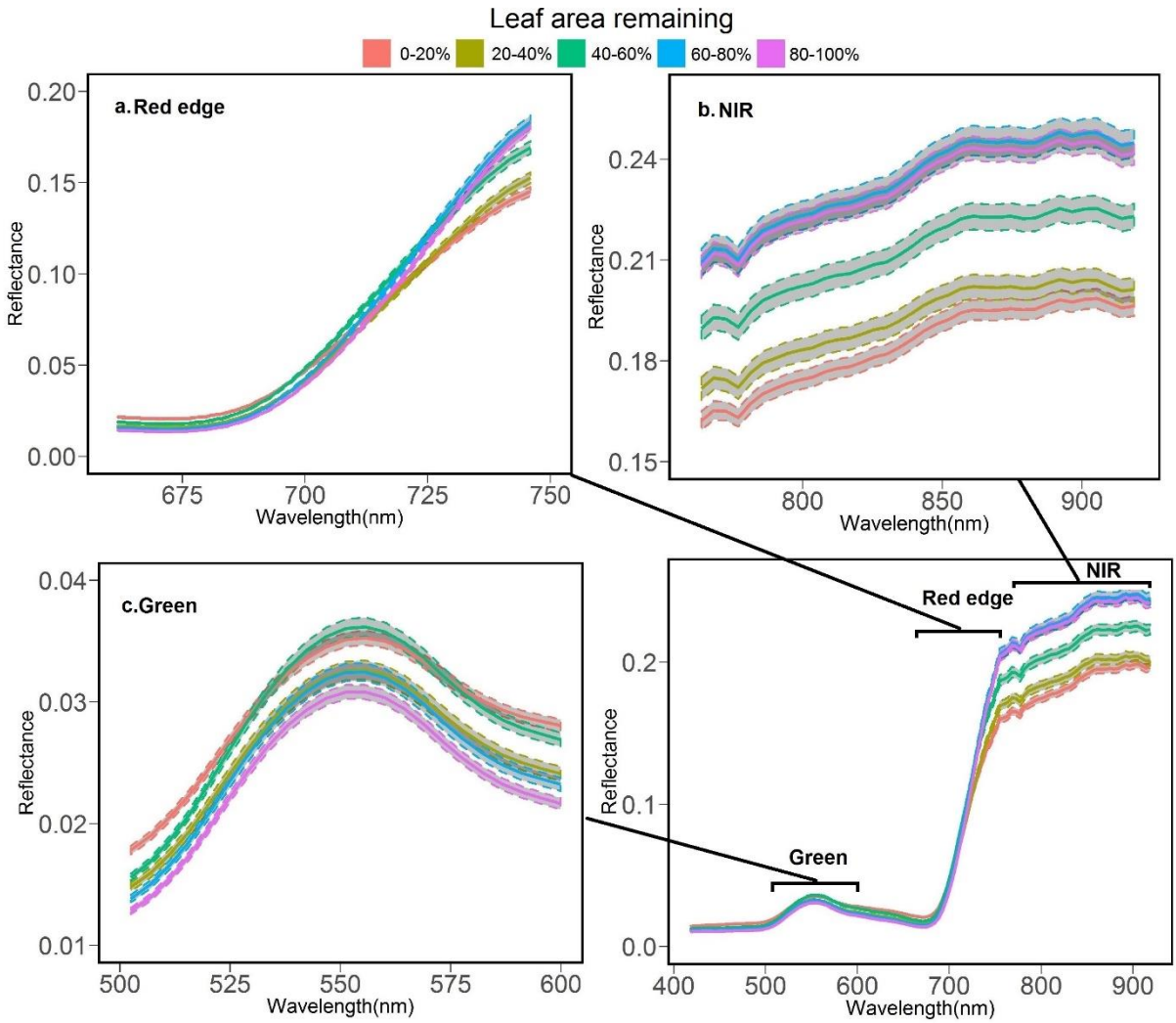

Figure 4. Mean crown-scale spectra and their 95% confidence interval for the following defoliation severity (i.e., percentage of leaf area remaining) groups extracted from the 2016 G-LiHT imaging spectroscopy measurement: 0-20% leaf area remaining; 20-40% leaf area remaining; 40-60% leaf area remaining; 60-80% leaf area remaining; 80-100% leaf area remaining; To avoid noise, percentage of leaf area remaining was grouped into 20% intervals, consistent with previous similar remote sensing studies (Townsend et al. 2012). (For interpretation of the references to color in this figure legend, the reader is referred to the web version of this article.)

4.2 Crown-scale structural changes by oak defoliation

LiDAR-measured canopy height profiles within the five defoliation severity groups varied from 2015 to 2016 (Fig. 6). Most of the defoliation severity groups had positive values at lower vertical height intervals (< 10m), indicating better penetration of laser pulses through the forest canopy in 2016 and returns from near the surface due to canopy leaf loss. Within the 10-20 m

349 vertical height interval, return points decreased from 2015 to 2016. However, there is no clear

350 trend within the 20-35 m vertical height interval.

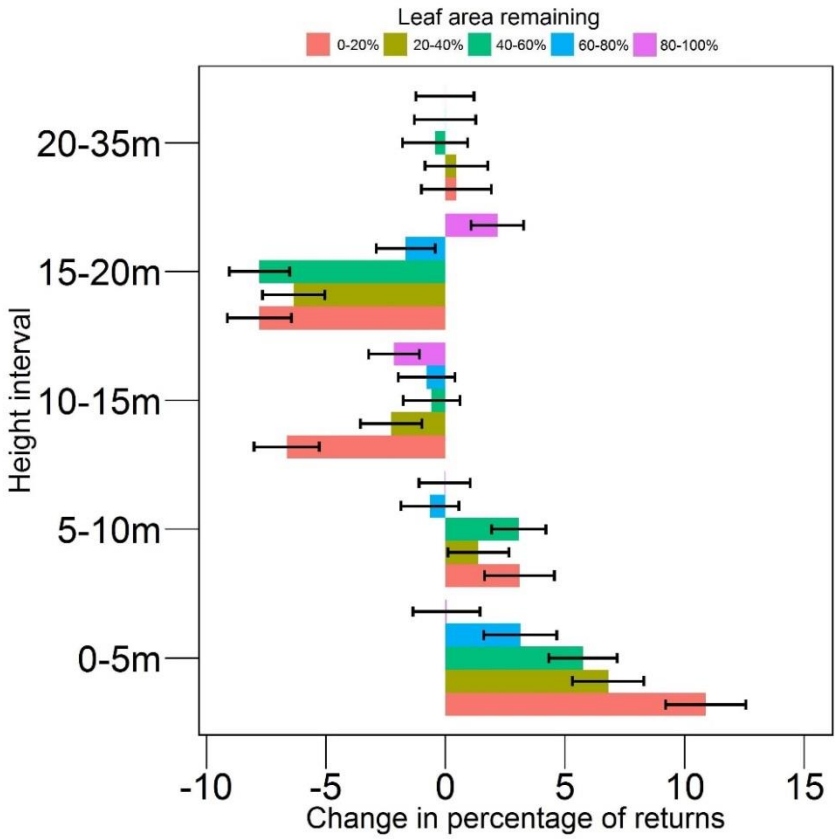

Figure 5. Change in canopy height profile within five defoliation severity (i.e., percentage of leaf area remaining) groups from 2015 to 2016 calculated from the G-LiHT LiDAR measurements; negative values indicate the decrease in vertical laser return point distributions from 2015 to 2016 at certain height interval, and positive values indicate the opposite trend; bars show the standard errors for each defoliation severity group. To avoid noise, percentage of leaf area remaining was grouped into 20% intervals, consistent with previous similar remote sensing studies (Townsend et al. 2012). (For interpretation of the references to color in this figure legend, the reader is referred to the web version of this article.)

4.3 Comparisons of OLS models using IS-only, LiDAR-only and IS+LiDAR variables

We plotted and compared the scatterplots of percentage of leaf area remaining versus 2016 IS and LiDAR metrics for variables with an absolute value of r >= 0.40 (Fig. 6). Among the 3 MESMA fraction and 31 LiDAR metrics, we selected all the MESMA and 11 of the LiDAR-derived predictors (Fig. 6). Specifically, all MESMA related predictors had an absolute value of r >= 0.40 with the percentage of leaf area remaining and were selected for further analysis; in terms of LiDAR-derived structural predictors, nearly all percentile height related predictors except B10 had relatively high linear correlations with crown-scale defoliation severity and demonstrated an increasing trend in correlation with percentile height (Fig. 6). We further calculated the changes from 2015 to 2016 for these predictors with an absolute value of r >= 0.40.

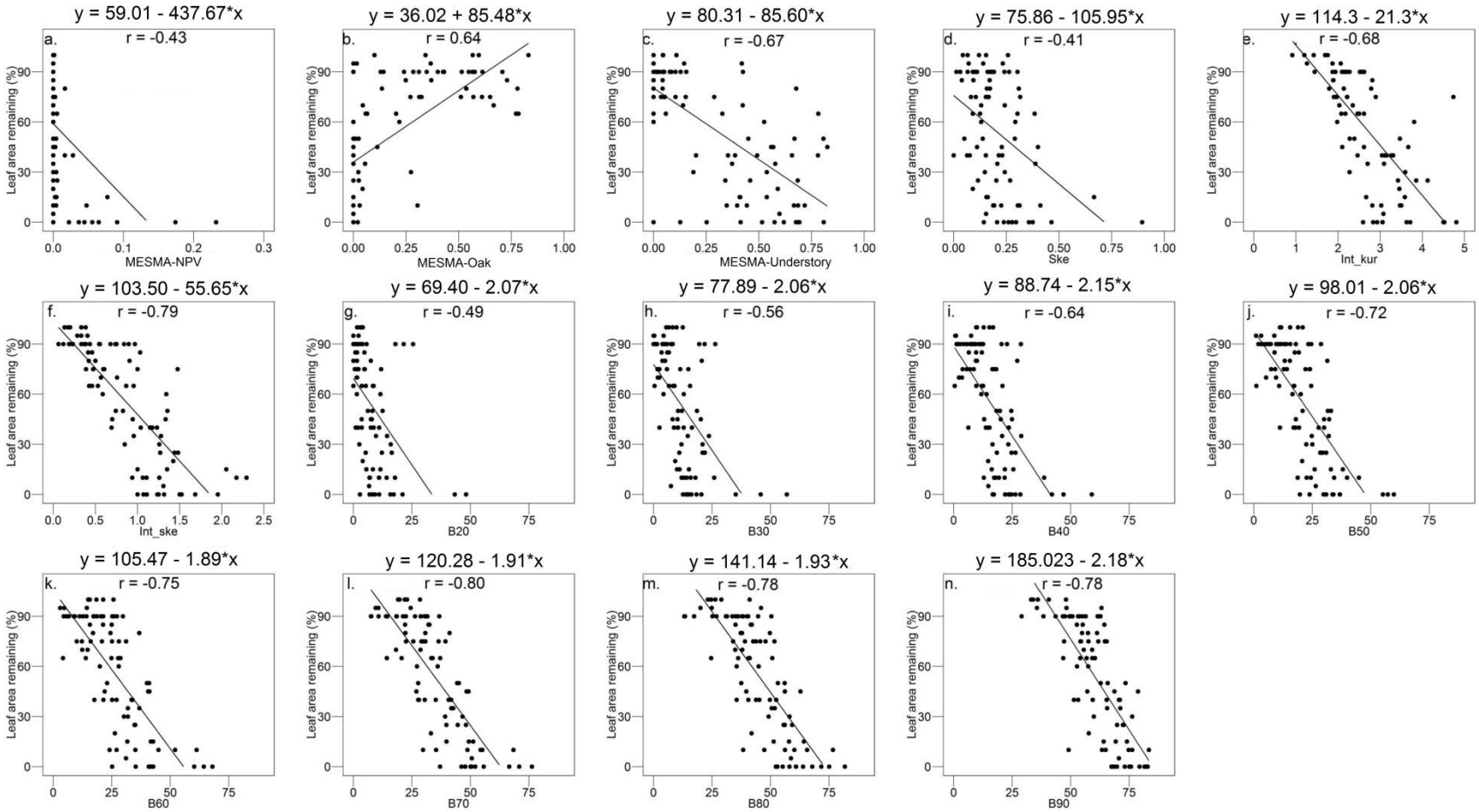

Figure 6. Scatter plot matrix of percentage of leaf area remaining vs. 2016 IS and LiDAR metrics used for model training: a. MESMA NPV fraction; b. MESMA oak fraction; c. MESMA understory fraction; d. LiDAR skewness; e. LiDAR Intensity kurtosis; f. LiDAR Intensity skewness; g. 20th bincentile height; h. 30th bincentile height; i. 40th bincentile height; j. 50th bincentile height; k. 60th bincentile height; l. 70th bincentile height; m.80th bincentile height; n. 90th bincentile height.

Based on the AIC metric, the most frequently selected important predictor variables differed among the IS-only, LiDAR-only and IS+LiDAR datasets (Table 2). Only the predictors selected more than 60 times were used for modeling canopy defoliation for each modeling option (i.e., IS-only, LiDAR-only, and IS+LiDAR; Table 2). Specifically, change in NPV fraction, oak fraction value in 2016, change in understory, and NPV fraction in 2016 were used for IS-only model; B70 in 2016, change in Kurtosis, and intensity skewness in 2016 were used for the LiDAR-only model; for the IS+LiDAR model, B70 in 2016, oak fraction value in 2016, and change in intensity skewness were used. We also calculated the 95% confidence interval of coefficient values of chosen predictors for each dataset option (Table 2).

Table 2 Selection frequencies of important predictor variables by AIC method during OLS modeling (only predictor variables selected more than once was shown here) and their confidence interval of coefficient values

Name	Frequency	Option	Chosen or not for final models	95% Confidence interval of coefficient values
Intercept				62.06 ± 0.74
Change in NPV fraction	100	IS-only	Yes	318.34 ± 8.61
Oak fraction in 2016	97	IS-only	Yes	35 ± 1.42
Change in understory fraction	95	IS-only	Yes	60.42 ± 1.25
NPV fraction in	86	IS-only	Yes	3058.67 ± 138.86

2016				
Change in MESMA oak fraction	9	IS-only	No	N.A.
MESMA understory fraction in 2016	6	IS-only	No	N.A.
Intercept		LiDAR-only		139.36 ± 0.7
B70 in 2016	99	LiDAR-only	Yes	-1.09 ± 0.02
Change in Kurtosis	70	LiDAR-only	Yes	-10.86 ± 0.35
Intensity skewness in 2016	60	LiDAR-only	Yes	-57.95 ± 0.65
Change in intensity skewness	16	LiDAR-only	No	N.A.
B80 in 2016	1	LiDAR-only	No	N.A.
Skewness in 2016	1	LiDAR-only	No	N.A.
Change in skewness	1	LiDAR-only	No	N.A.
Intercept		IS+LiDAR		100.53 ± 0.3
B70 in 2016	98	IS+LiDAR	Yes	-1.12 ± 0.02
MESMA Oak fraction in 2016	97	IS+LiDAR	Yes	36.28 ± 0.8
Change in intensity skewness	69	IS+LiDAR	Yes	20.82 ± 0.57

Change in Kurtosis	38	IS+LiDAR	No	N.A.
Intensity skewness in 2016	13	IS+LiDAR	No	N.A.
Change in B80	8	IS+LiDAR	No	N.A.
MESMA NPV fraction in 2016	2	IS+LiDAR	No	N.A.
Change in MESMA NPV fraction	1	IS+LiDAR	No	N.A.

373 Validation results varied among the three predictor options (Fig. 7). Overall, the IS-only model
374 had the lowest mapping accuracy with a mean Adj. R value of 0.63, significantly lower ($P <$
375 0.001) than LiDAR-only and IS + LiDAR models. The validation accuracy of the IS + LiDAR
376 model was only slightly higher than that of LiDAR model (0.81 vs. 0.77), but still statistically
377 significant at the level of 0.05. Using RMSE as a metric, the IS+LiDAR model consistently
378 performed best for mapping canopy defoliation (14.46 ±2.22%), comparing with the IS-only
379 model (19.11±2.90%) and the LiDAR-only model (15.37±2.12%). Moreover, the value ranges of
380 Adj.R-squared and RMSE (%) for LiDAR-only and IS+LiDAR model were both much less (i.e.
381 50% and 30%, respectively) than that for IS-only model, signifying much lower modeling
382 uncertainty (Fig.S1). Finally, we found regression coefficients from the different dataset splitting
383 schemes were consistent, in terms of their general pattern and relative magnitude (Table 2).

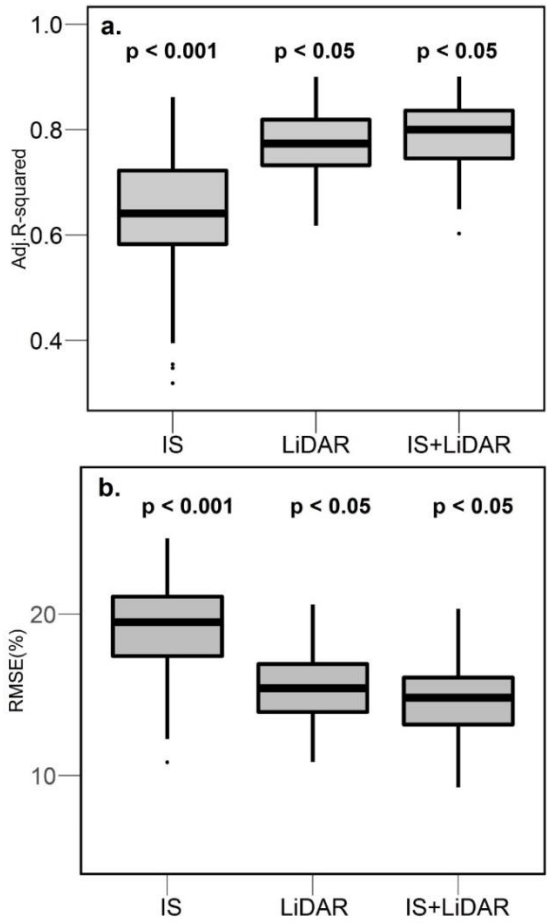

Figure 7. Boxplots of adjusted R-squared (a) and RMSE (b) values using IS-only predictor variables, LiDAR-only predictor variables and their combination for predicting canopy defoliation of validation datasets. p values show the least significance of paired Wilcoxon signed rank test results.

4.4 Biophysical effects of canopy defoliation

To explore the biophysical effects underpinning the spectral and structural signatures of oak defoliation, we summarized the MESMA fraction values and LiDAR metrics in 2015 and 2016 within the five defoliation severity groups (Figs. 8 and 9). Oak fractional cover generally decreased from 2015 to 2016, but understory and NPV fractional cover indicated the opposite trend (Fig. 8). Specifically, IS measurement captured the increased exposure of forest understory (i.e., shrubs) and NPV materials (i.e., trunk and branch), as a result of decrease in canopy leaf area. More importantly, these changes varied with the defoliation severity, with the largest changes found in highest severity groups (0-20% leaf area remaining). Thus, we conclude that the detected crown-scale spectral and structural signatures in Section 4.1 & 4.2 can be explained

by biophysical effects of insect herbivory including decrease in canopy leaf area and increased exposure in NPV and understory. For LiDAR metrics, B70 (70th bincentile height, Table 1), intensity skewness, and kurtosis all increased from 2015 to 2016, but their change magnitudes decreased with defoliation severity (Fig. 9). These trends are consistent with changes in the canopy height profile within five defoliation severity groups (Fig. 5).

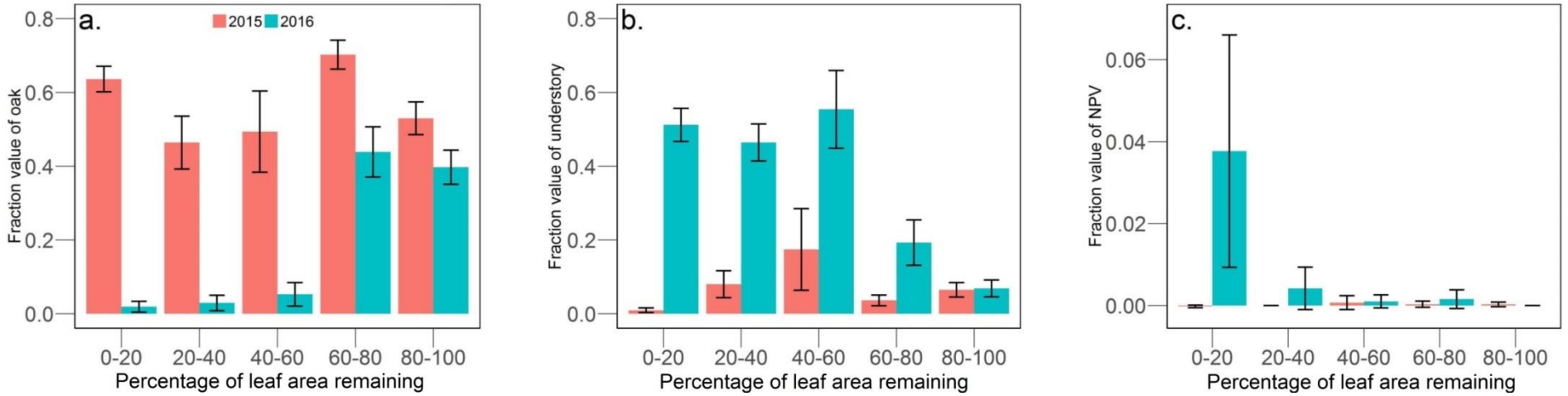

Figure 8. Average and standard error values of MESMA fractions at five leaf area remaining (i.e., canopy defoliation severity) groups for 2015 and 2016: a. GV-oak fraction; b. GV-understory fraction; c. NPV fraction. (For interpretation of the references to color in this figure legend, the reader is referred to the web version of this article.)

399

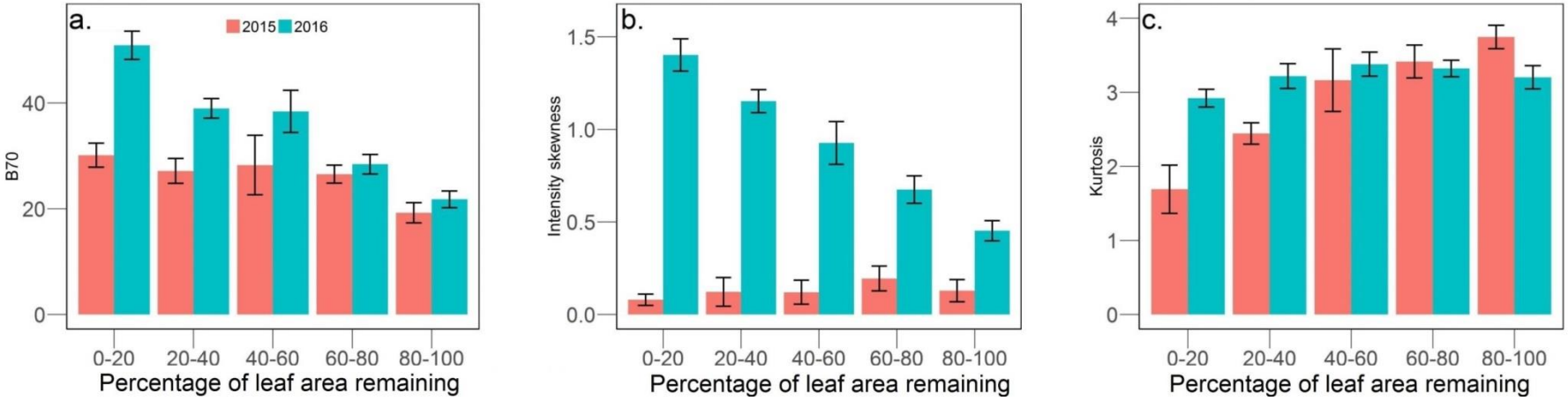

Figure 9. Average and standard error values of LiDAR predictors selected by stepwise AIC-based method (see Section 4.4) for mapping crown-scale canopy defoliation at five leaf area remaining (i.e., canopy defoliation severity) groups for 2015 and 2016: a. B70; b. Intensity skewness; c. Kurtosis.(For interpretation of the references to color in this figure legend, the reader is referred to the web version of this article.)

400 **4.5 Crown-scale canopy defoliation across the study area**

401 The final used IS+LiDAR model for mapping crown-scale oak defoliation across the study area
402 was as below.

403 $$C_d\ (\%) = 100.53 + 36.28 \times M_{oak,2016} - 1.12 \times B70_{2016} + 20.82 \times Skewness_c \quad \text{Eq. 2}$$

404 Where C_d stands for percentage of leaf area remaining, $M_{oak,2016}$ for MESMA oak fraction in
405 2016, $B70_{2016}$ for B70 in 2016, and $Skewness_c$ for change in intensity skewness from 2015 to
406 2016. It was possible for our model to produce percentage of leaf area remaining less than 0% or
407 greater than 100%. In these cases, we reset the modeled value to the closest physically possible
408 value (0% or 100%). We also split the continuous measurements of percentage of leaf area
409 remaining by the IS + LiDAR model into five groups for map display.

410 We applied Eq. 2 to the G-LiHT IS+LiDAR dataset covering our study area to map the spatial
411 patterns of canopy leaf status associated with gypsy moth outbreak in 2016 (Fig. 10).
412 Defoliation was scattered in the 2016 map, with large patches of heavy defoliation (0-20% leaf
413 area remaining or 80-100% canopy leaf loss). 2.0% of crown objects suffered heavy defoliation,
414 which is equivalent to 104,811 m2 of canopy area in our study area. The MEMSA oak fraction,
415 ranging between 0 to 1, and LiDAR B70, ranging between 0 to 100%, corresponded well with
416 the spatial pattern of modeled canopy defoliation status (percentage of leaf area remaining) in
417 our study areas.

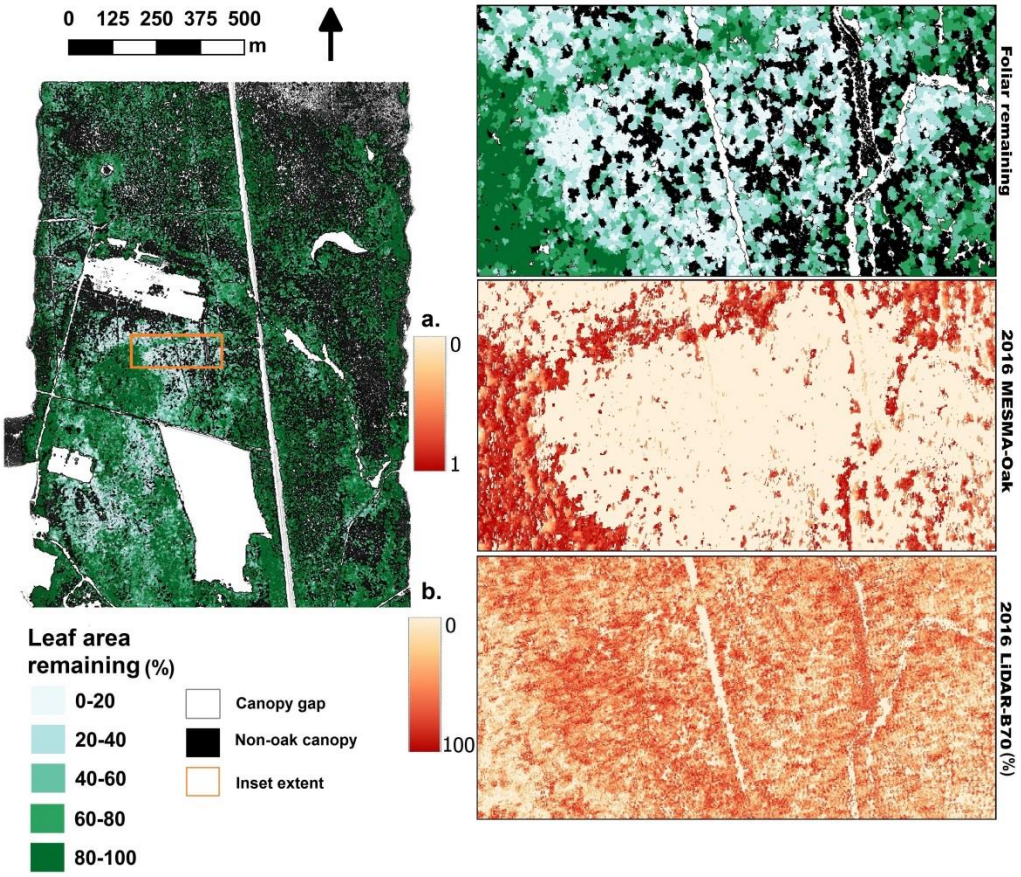

Figure 10. Crown-scale percentage of oak leaf area remaining (i.e., oak canopy defoliation severity) map at 1m resolution in a mixed pine-oak forest, Long island, NY in 2016; the inset subplots show a partial zoom-in view of the defoliation severity map and corresponding MESMA oak fraction (a) and LiDAR-derived B70 (i.e., 70th bincentile height) (b). The rectangle on the oak canopy defoliation severity map shows the inset extent. (For interpretation of the references to color in this figure legend, the reader is referred to the web version of this article.)

5 Discussion

High resolution canopy defoliation mapping is critical for monitoring and exploring the effects of insect infestations on forest health and ecosystem dynamics, particularly under drier and warmer climate scenarios that may weaken tree defenses to insect attack (Hicke et al. 2012; Seidl et al. 2014; Seidl et al. 2017). We leveraged co-aligned VHR airborne optical IS and structural LiDAR measurements to map defoliation by gypsy moth caterpillars at the individual tree level.

We found crown-scale oak spectra at red-edge and NIR wavelengths were most sensitive to defoliation severity, and simple LiDAR metrics (e.g., B70, intensity skewness, and Kurtosis) can effectively detect the crown-scale overall structural changes caused by herbivorous insects. Biophysical effects of canopy leaf loss, particularly exposed understory and NPV, underpinned the detected spectral and structural changes across the defoliation severity gradient. Lastly, we found an IS+LiDAR OLS model had the best mapping performance (Fig. 9) among three predictor options (IS-only, LiDAR-only, and IS+LiDAR), with LiDAR-only outperforming IS-only. We didn't account for spatial effects for the OLS modeling of canopy defoliation in our study, because spatial modeling techniques, such as autoregressive model and spatial filtering (McCarley et al. 2017; Meng et al. 2015), might further improve the accuracy of OLS training models, but would increase the uncertainty of applying the trained model to the whole study area.

Our analysis is distinguished from the previous studies in that we explored the combined hyperspectral and LiDAR-derived structural signatures of deciduous broadleaved trees across a defoliation severity gradient at the individual tree level. Most previous efforts have focused on analyzing spectral signatures of defoliation severity or mortality at >=30 m plot (i.e., inter-stand) scale with broadband multi-spectral sensors (Radeloff et al. 1999; Rullan-Silva et al. 2013; Senf et al. 2015; Senf et al. 2017c; Townsend et al. 2012), but previous studies also indicate that the pattern of insect outbreak is driven by multi-scale processes (Seidl et al. 2016; Senf et al. 2017a). Thus this study has filled in an important knowledge gap in crown-scale spectral and structural signatures of defoliation severity and provides the groundwork for consistently mapping defoliation severity across multiple scales, which are critical for forest management and ecological study, as well as for informing and testing of carbon cycle models (Clark et al. 2010; Landry et al. 2016; McDowell et al. 2015; Seidl et al. 2016; Senf et al. 2017a). Specifically, our

study indicates that the combined use of VHR IS and LiDAR measurements can provide an opportunity to scale remotely sensed measurements of defoliation severity from the individual-tree level to inter-stand level: on one hand, further studies can be conducted to determine to what extent crown-scale canopy defoliation contributed to the inter-stand scale change in spectral reflectance of broadband multi-spectral sensors like Landsat-8 and Sentinel-2 with higher temporal resolution and larger spatial coverage (Senf et al. 2015; Townsend et al. 2012; Zarco-Tejada et al. 2018); on the other hand, our results can be used to separate the signature of canopy defoliation from other temporal changes (e.g., phenology) that may be present in Landsat or Sentinel-2 data (Hawryło et al. 2018; Senf et al. 2017b). The improved capabilities of remote sensing of insect outbreak at crown-scale can provide new insights for reducing insect habitat quantity and quality and understanding insect outbreak's mechanic process (McDowell et al. 2015; Senf et al. 2017a).

Our study found a negative relationship between NIR reflectance and defoliation severity (Fig. 2), and this relationship is consistent with relationships found by previous studies investigating defoliation of conifers and spruce at inter-stand scale with broadband multi-spectral sensors (Ahern 1988; Olsson et al. 2012), but different from an increase in NIR reflectance following insect outbreak in jack pine (Radeloff et al. 1999). Our VHR results further indicate that NPV and the forest understory, which were not considered in previous studies, can also affect remotely sensed measurements of oak defoliation and should be taken into account for canopy defoliation mapping, in addition to canopy leaf area (Figs. 6 & 8). The differences in forest understory and structure in varied forest ecosystems can likely explain differences in spectral changes after the insect outbreak across previous studies (Ahern 1988; Griffiths et al. 2014; Olsson et al. 2012; Radeloff et al. 1999) and the defoliation severity model (Eq. 2) developed

here would have to be adapted for forests with different forest structure, composition and understories. Moreover, our analysis was based on 91 oak crowns in a local forest and segmentation parameters for crown delineations used here (see Section 3.1) can also change with forest type, which further adds to uncertainties in the generalized use of our derived defoliation severity model (Eq. 2). We thus recommend more spectral and structural signature studies of canopy defoliation across severity gradients at VHR in other forest ecosystems for studying scaling effects and consistent modeling of canopy defoliation across large spatial-temporal scales.

Most previous remote sensing studies of canopy defoliation have focused on the spectral index-based methods (Rullan-Silva et al. 2013; Senf et al. 2017c), which are simple and easy to implement. We have tested the suitability of available visible-NIR narrowband spectral indices in G-LiHT IS data for mapping defoliation severity (Table S2). This analysis demonstrated that red edge indices, such as Modified Red Edge Normalized Difference Vegetation Index (MENDVI) and Vogelmann Red Edge Index 1 (VREI1), had the highest correlations with canopy defoliation caused by insect outbreak (Table S2), which is consistent with previous similar studies (Hawryło et al. 2018; Knipling 1970; Oumar and Mutanga 2014; Rock et al. 1988; Shendryk et al. 2016; Townsend et al. 2012). Similar results were also reported in Shendryk et al. (2016), where IS-derived red-edge and NIR variables were the most important ones in predicting tree dieback and defoliation caused by flooding. With the increasing availability of red edge and even shortwave infrared (SWIR) bands on spaceborne remote sensing platforms (i.e., VHR Worldview-3 and moderate-resolution Sentinel-2) (Drusch et al. 2012; Warner et al. 2017), more accurate mapping of spatial variation in defoliation severity is promising with these new sensors. Additionally, given the apparent advantages of narrowband vegetation indices and potential for full spectrum metrics like fractional cover, future spaceborne IS mission sensors (e.g., HyspIRI

and EnMap) could further improve our capability for mapping insect defoliation despite coarser spatial resolution (Lee et al. 2015; Stuffler et al. 2007). In summary, these mentioned new sensors could potentially enable improved monitoring of the spread and severity of forest infestations across scales, forest types, and disturbance agents with higher accuracy and frequency than ever before. But the G-LiHT IS used here does not cover the SWIR wavelengths, which are sensitive to leaf water content and lignocellulose absorption and have been widely used for remote sensing of canopy defoliation (Somers et al. 2010; Townsend et al. 2012). Metrics using SWIR bands made available by these recent and the planned sensors at moderate spatial resolution thus still require further study to compare their predictive power with LiDAR-derived metrics chosen in this study (Fig. 9). However, previous studies also indicate that visible-NIR wavelengths are still viable for mapping canopy defoliation, in absence of SWIR wavelengths (Townsend et al. 2012).

To examine whether LiDAR can be used for measuring defoliation severity of broadleaf deciduous trees, we explored the sensitivity of various LiDAR metrics to the change in overall canopy structure caused by herbivorous insects. Previous studies have explored remote sensing of fire-induced structural changes or beetle-induced conifer leaf loss using LiDAR (Alonzo et al. 2017; Hanssen and Solberg 2007; McCarley et al. 2017; Solberg et al. 2006), but few studies examined the capability of LiDAR metrics for measuring insect-induced broadleaf deciduous tree defoliation severity at the individual tree level. Our analysis shows that simple LiDAR metrics, such as B70 (i.e.,70th bincentile height), intensity skewness and kurtosis, are sensitive to canopy leaf loss by herbivorous insects across the defoliation severity gradient (Fig. 9). This can be explained by the fact that canopy leaf loss by herbivorous insects can increase the chance of LiDAR pulses to penetrate the tree canopies and rebound from the understory, leading to

somewhat large variations in vertical profiles of return points, which can increase the LiDAR intensity skewness and kurtosis (Figs. 5 & 9). Additionally, defoliation should provide a distinctive structural signature when compared to fire or logging disturbance (Bolton et al. 2017; Bolton et al. 2015; Kane et al. 2014; Zhao et al. 2015), since insect herbivory doesn't affect branch, trunk, and understory returns. LiDAR data thus may be uniquely capable of mapping different disturbance types based on their structural fingerprint. With the future global LiDAR coverage provided by the Global Ecosystem Dynamics Investigation (GEDI) mission (Dubayah et al. 2014), there is potential to scale up crown-scale measurements of defoliation provided by airborne LiDAR data.

Using airborne IS and LiDAR imaging, our study provides a rapid and accurate approach for regional defoliation severity mapping at the individual tree level. Our validation results of three predictor options (Fig. 9 and Fig.S1) indicate that the combination of IS and LiDAR provide more additional information for mapping defoliation by herbivorous insects than using either sensor type alone, and the LiDAR-only OLS model outperformed the IS-only model, demonstrating that if only one data type could be collected, LiDAR would provide the better ability to map canopy defoliation severity of broadleaf trees. As the development of unmanned remote sensing techniques and computer vision (e.g., Structure from Motion algorithm for three dimensional information construction from two-dimensional image sequences) continues (Alonzo et al. 2018; Colomina and Molina 2014), the cost of aerial surveys can be further reduced and more studies can be potentially conducted in multiple representative forest ecosystems to scale crown-level defoliation measurements to the inter-stand level, enabling real-time monitoring of canopy defoliation at regional and global scales (Dash et al. 2017; Pasquarella et al. 2017). Considering forest damage caused by herbivorous insects is a function

of both the severity and timing of defoliation, more frequent and more accurate spatial-temporal measurements of canopy defoliation are critical to better assisting forest managers with designing adaptive management strategies for reducing forest damage and maintaining forest health. Additionally, the derived high resolution spatial-temporal information would be also essential for exploring insect herbivory effects on ecosystem functioning, diversity, and carbon dynamics (de la Mata et al. 2017; Frost and Hunter 2004; Goetz et al. 2012; Kenis et al. 2009; Townsend et al. 2004).

6 Conclusion

We explored the crown-level spectral and structural signatures of canopy defoliation by herbivorous insects, as well as underlying biophysical effects, across a defoliation severity gradient using bi-temporal airborne IS and LiDAR measurements. Our results showed that: (1) red edge and NIR spectra are most sensitive to crown-level defoliation severity; (2) LiDAR metrics including B70, intensity skewness, and intensity kurtosis can effectively detect overall canopy structural changes by herbivorous insects and thus can be used for mapping canopy defoliation; (3) In addition to canopy leaf loss, crown-scale biophysical effects of insect herbivory also included increased exposure of understory (e.g., shrub) and NPV (e.g., branch and trunk), which can affect the overall spectral and structural signatures; (4) the IS + LiDAR OLS model (Adj. R-squared = 0.81, RMSE = 14.46%) performed better for measuring canopy defoliation severity than the IS-only (Adj. R-squared = 0.63, RMSE = 19.11%) or LiDAR-only OLS models (Adj. R-squared = 0.77, RMSE = 15.37%). Our aerial survey-based approach, in combination with the current and next generation of spaceborne sensors (e.g., Landsat-8, HyspIRI, EnMap, GEDI, WorldView-3, Sentinel-2), can provide critical information on canopy defoliation over large spatial-temporal scales and thus improve our understanding of the

ecological and economic consequences of forest infestations (e.g., reduced growth and increased mortality), as well as implications for forest carbon dynamics. This study serves as one of first efforts for understanding VHR spectral and structural signatures of gypsy moth-caused defoliation in a mixed oak-pine forest, and future work should focus on extending our proposed framework to other types of forests and defoliators/pests.

7 Acknowledgement

This work was supported by the United States Department of Energy contract No. DE-SC0012704 to Brookhaven National Laboratory. We also thank Dr. Jin Wu for discussions.

References

Ahern, F.J. (1988). The effects of bark beetle stress on the foliar spectral reflectance of lodgepole pine. *International Journal of Remote Sensing, 9*, 1451-1468

Alonzo, M., Andersen, H.-E., Morton, D.C., & Cook, B.D. (2018). Quantifying Boreal Forest Structure and Composition Using UAV Structure from Motion. *Forests, 9*, 119

Alonzo, M., Morton, D.C., Cook, B.D., Andersen, H.-E., Babcock, C., & Pattison, R. (2017). Patterns of canopy and surface layer consumption in a boreal forest fire from repeat airborne lidar

Asner, G.P., Martin, R.E., Knapp, D.E., Tupayachi, R., Anderson, C.B., Sinca, F., Vaughn, N.R., & Llactayo, W. (2017). Airborne laser-guided imaging spectroscopy to map forest trait diversity and guide conservation. *Science, 355*, 385-388

Ayres, M.P., & Lombardero, M.a.J. (2000). Assessing the consequences of global change for forest disturbance from herbivores and pathogens. *Science of the Total Environment, 262*, 263-286

Black, S.H. (2005). Logging to Control Insects: The Science and Myths Behind Managing Forest Insect Pests. *A synthesis of independently reviewed research. Portland: The Xerces Society for Invertebrate Conservation*

585 Bolton, D.K., Coops, N.C., Hermosilla, T., Wulder, M.A., & White, J.C. (2017). Assessing variability in
586 post‐fire forest structure along gradients of productivity in the Canadian boreal using multi‐source
587 remote sensing. *Journal of Biogeography*

588 Bolton, D.K., Coops, N.C., & Wulder, M.A. (2015). Characterizing residual structure and forest recovery
589 following high-severity fire in the western boreal of Canada using Landsat time-series and airborne lidar
590 data. *Remote Sensing of Environment, 163*, 48-60

591 Burnham, K.P., & Anderson, D.R. (2004). Multimodel inference: understanding AIC and BIC in model
592 selection. *Sociological methods & research, 33*, 261-304

593 Clark, K.L., Skowronski, N., & Hom, J. (2010). Invasive insects impact forest carbon dynamics. *Global*
594 *Change Biology, 16*, 88-101

595 Colomina, I., & Molina, P. (2014). Unmanned aerial systems for photogrammetry and remote sensing: A
596 review. *ISPRS Journal of Photogrammetry and Remote Sensing, 92*, 79-97

597 Cook, B.D., Nelson, R.F., Middleton, E.M., Morton, D.C., McCorkel, J.T., Masek, J.G., Ranson, K.J., Ly, V., &
598 Montesano, P.M. (2013). NASA Goddard's lidar, hyperspectral and thermal (G-LiHT) airborne imager.
599 *Remote Sensing, 5*, 4045-4066

600 Coulson, R.N., McFadden, B.A., Pulley, P.E., Lovelady, C.N., Fitzgerald, J.W., & Jack, S.B. (1999).
601 Heterogeneity of forest landscapes and the distribution and abundance of the southern pine beetle.
602 *Forest ecology and management, 114*, 471-485

603 Coyle, D.R., Hart, E.R., McMillin, J.D., Rule, L.C., & Hall, R.B. (2008). Effects of repeated cottonwood leaf
604 beetle defoliation on Populus growth and economic value over an 8-year harvest rotation. *Forest*
605 *ecology and management, 255*, 3365-3373

606 Dale, V.H., Joyce, L.A., McNulty, S., Neilson, R.P., Ayres, M.P., Flannigan, M.D., Hanson, P.J., Irland, L.C.,
607 Lugo, A.E., Peterson, C.J., Simberloff, D., Swanson, F.J., Stocks, B.J., & Wotton, B.M. (2001). Climate
608 change and forest disturbances. *BioScience, 51*, 723-734

609 Dash, J.P., Watt, M.S., Pearse, G.D., Heaphy, M., & Dungey, H.S. (2017). Assessing very high resolution
610 UAV imagery for monitoring forest health during a simulated disease outbreak. *ISPRS Journal of*
611 *Photogrammetry and Remote Sensing, 131*, 1-14

De Beurs, K.M., & Townsend, P.A. (2008). Estimating the effect of gypsy moth defoliation using MODIS. *Remote Sensing of Environment, 112*, 3983-3990

de la Mata, R., Hood, S., & Sala, A. (2017). Insect outbreak shifts the direction of selection from fast to slow growth rates in the long-lived conifer Pinus ponderosa. *Proceedings of the National Academy of Sciences*, 201700032

Dennison, P.E., Brunelle, A.R., & Carter, V.A. (2010). Assessing canopy mortality during a mountain pine beetle outbreak using GeoEye-1 high spatial resolution satellite data. *Remote Sensing of Environment, 114*, 2431-2435

Dennison, P.E., Nagler, P.L., Hultine, K.R., Glenn, E.P., & Ehleringer, J.R. (2009). Remote monitoring of tamarisk defoliation and evapotranspiration following saltcedar leaf beetle attack. *Remote Sensing of Environment, 113*, 1462-1472

Drake, N.A., Mackin, S., & Settle, J.J. (1999). Mapping vegetation, soils, and geology in semiarid shrublands using spectral matching and mixture modeling of SWIR AVIRIS imagery. *Remote Sensing of Environment, 68*, 12-25

Drusch, M., Del Bello, U., Carlier, S., Colin, O., Fernandez, V., Gascon, F., Hoersch, B., Isola, C., Laberinti, P., & Martimort, P. (2012). Sentinel-2: ESA's optical high-resolution mission for GMES operational services. *Remote Sensing of Environment, 120*, 25-36

Dubayah, R., Goetz, S.J., Blair, J.B., Fatoyinbo, T.E., Hansen, M., Healey, S.P., Hofton, M.A., Hurtt, G.C., Kellner, J., & Luthcke, S.B. (2014). The global ecosystem dynamics investigation. In

Dudley, T.L., & Bean, D.W. (2012). Tamarisk biocontrol, endangered species risk and resolution of conflict through riparian restoration. *BioControl, 57*, 331-347

Elkinton, J.S., & Liebhold, A.M. (1990). Population dynamics of gypsy moth in North America. *Annual review of entomology, 35*, 571-596

Fassnacht, F.E., Latifi, H., Ghosh, A., Joshi, P.K., & Koch, B. (2014). Assessing the potential of hyperspectral imagery to map bark beetle-induced tree mortality. *Remote Sensing of Environment, 140*, 533-548

638 Foster, J.R., Townsend, P.A., & Mladenoff, D.J. (2013). Spatial dynamics of a gypsy moth defoliation
639 outbreak and dependence on habitat characteristics. *Landscape ecology, 28*, 1307-1320

640 Franklin, S.E., Fan, H., & Guo, X. (2008). Relationship between Landsat TM and SPOT vegetation indices
641 and cumulative spruce budworm defoliation. *International Journal of Remote Sensing, 29*, 1215-1220

642 Frost, C.J., & Hunter, M.D. (2004). Insect canopy herbivory and frass deposition affect soil nutrient
643 dynamics and export in oak mesocosms. *Ecology, 85*, 3335-3347

644 Gandhi, K.J.K., & Herms, D.A. (2010). Direct and indirect effects of alien insect herbivores on ecological
645 processes and interactions in forests of eastern North America. *Biological Invasions, 12*, 389-405

646 Ghasemi, A., & Zahediasl, S. (2012). Normality tests for statistical analysis: a guide for non-statisticians.
647 *International journal of endocrinology and metabolism, 10*, 486

648 Goetz, S.J., Bond‐Lamberty, B., Law, B.E., Hicke, J.A., Huang, C., Houghton, R.A., McNulty, S., O'Halloran,
649 T., Harmon, M., & Meddens, A.J.H. (2012). Observations and assessment of forest carbon dynamics
650 following disturbance in North America. *Journal of Geophysical Research: Biogeosciences, 117*

651 Griffith, D.A. (2009). Spatial Autocorrelation. In K. Editors-in-Chief: Rob, & T. Nigel (Eds.), *International*
652 *Encyclopedia of Human Geography* (pp. 308-316). Oxford: Elsevier

653 Griffiths, P., Kuemmerle, T., Baumann, M., Radeloff, V.C., Abrudan, I.V., Lieskovsky, J., Munteanu, C.,
654 Ostapowicz, K., & Hostert, P. (2014). Forest disturbances, forest recovery, and changes in forest types
655 across the Carpathian ecoregion from 1985 to 2010 based on Landsat image composites. *Remote*
656 *Sensing of Environment, 151*, 72-88

657 Hanavan, R.P., Pontius, J., & Hallett, R. (2015). A 10-Year assessment of hemlock decline in the catskill
658 mountain region of new York state using hyperspectral remote sensing techniques. *Journal of economic*
659 *entomology, 108*, 339-349

660 Hanssen, K.H., & Solberg, S. (2007). Assessment of defoliation during a pine sawfly outbreak: Calibration
661 of airborne laser scanning data with hemispherical photography. *Forest Ecology and Management, 250*,
662 9-16

663 Hawryło, P., Bednarz, B., Wężyk, P., & Szostak, M. (2018). Estimating defoliation of Scots pine stands
664 using machine-learning methods and vegetation indices of Sentinel-2. *European Journal of Remote*
665 *Sensing, 51*, 194-204

666 Hicke, J.A., Allen, C.D., Desai, A.R., Dietze, M.C., Hall, R.J., Hogg, E.H., Kashian, D.M., Moore, D., Raffa,
667 K.F., Sturrock, R.N., & Vogelmann, J. (2012). Effects of biotic disturbances on forest carbon cycling in the
668 United States and Canada. *Global Change Biology, 18*, 7-34

669 Hurley, A., Watts, D., Burke, B., & Richards, C. (2004). Identifying gypsy moth defoliation in Ohio using
670 Landsat data. *Environmental & Engineering Geoscience, 10*, 321-328

671 Ji, W.J., Wang, L., & Knutson, A.E. (2017). Detection of the spatiotemporal patterns of beetle-induced
672 tamarisk (Tamarix spp.) defoliation along the Lower Rio Grande using Landsat TM images. *Remote*
673 *Sensing of Environment, 193*, 76-85

674 Kane, V.R., Cansler, C.A., Povak, N.A., Kane, J.T., McGaughey, R.J., Lutz, J.A., Churchill, D.J., & North, M.P.
675 (2015). Mixed severity fire effects within the Rim fire: Relative importance of local climate, fire weather,
676 topography, and forest structure. *Forest Ecology and Management, 358*, 62-79

677 Kane, V.R., North, M.P., Lutz, J.A., Churchill, D.J., Roberts, S.L., Smith, D.F., McGaughey, R.J., Kane, J.T., &
678 Brooks, M.L. (2013). Assessing fire effects on forest spatial structure using a fusion of Landsat and
679 airborne LiDAR data in Yosemite National Park. *Remote Sensing of Environment*

680 Kane, V.R., North, M.P., Lutz, J.A., Churchill, D.J., Roberts, S.L., Smith, D.F., McGaughey, R.J., Kane, J.T., &
681 Brooks, M.L. (2014). Assessing fire effects on forest spatial structure using a fusion of Landsat and
682 airborne LiDAR data in Yosemite National Park. *Remote Sensing of Environment, 151*, 89-101

683 Kantola, T., Vastaranta, M., Yu, X., Lyytikainen-Saarenmaa, P., Holopainen, M., Talvitie, M., Kaasalainen,
684 S., Solberg, S., & Hyyppa, J. (2010). Classification of defoliated trees using tree-level airborne laser
685 scanning data combined with aerial images. *Remote sensing, 2*, 2665-2679

686 Kautz, M., Anthoni, P., Meddens, A.J.H., Pugh, T.A.M., & Arneth, A. (2017a). Simulating the recent
687 impacts of multiple biotic disturbances on forest carbon cycling across the United States. *Global change*
688 *biology*

689 Kautz, M., Meddens, A.J.H., Hall, R.J., & Arneth, A. (2017b). Biotic disturbances in Northern Hemisphere
690 forests - a synthesis of recent data, uncertainties and implications for forest monitoring and modelling.
691 *Global Ecology and Biogeography, 26*, 533-552

692 Kegg, J.D. (1971). The impact of gypsy moth: repeated defoliation of oak in New Jersey. *Journal of*
693 *Forestry, 69*, 852-854

694 Kenis, M., Auger-Rozenberg, M.-A., Roques, A., Timms, L., Péré, C., Cock, M.J.W., Settele, J., Augustin, S.,
695 & Lopez-Vaamonde, C. (2009). Ecological effects of invasive alien insects. *Biological Invasions, 11*, 21-45

696 Knipling, E.B. (1970). Physical and physiological basis for the reflectance of visible and near-infrared
697 radiation from vegetation. *Remote Sensing of Environment, 1*, 155-159

698 Kolb, T.E., Fettig, C.J., Ayres, M.P., Bentz, B.J., Hicke, J.A., Mathiasen, R., Stewart, J.E., & Weed, A.S.
699 (2016). Observed and anticipated impacts of drought on forest insects and diseases in the United States.
700 *Forest Ecology and Management, 380*, 321-334

701 Kurczewski, F.E., & Boyle, H.F. (2000). Historical changes in the pine barrens of central Suffolk County,
702 New York. *Northeastern Naturalist, 7*, 95-112

703 Landry, J.S., Price, D.T., Ramankutty, N., Parrott, L., & Matthews, H.D. (2016). Implementation of
704 a Marauding Insect Module (MIM, version 1.0) in the Integrated BIosphere Simulator (IBIS, version 2.6b4)
705 dynamic vegetation–land surface model. *Geosci. Model Dev., 9*, 1243-1261

706 Landsber, J., & Ohmart, C. (1989). Levels of insect defoliation in forests: patterns and concepts. *Trends in*
707 *Ecology & Evolution, 4*, 96-100

708 Lausch, A., Erasmi, S., King, D.J., Magdon, P., & Heurich, M. (2016). Understanding forest health with
709 remote sensing-part I—a review of spectral traits, processes and remote-sensing characteristics. *Remote*
710 *Sensing, 8*, 1029

711 Lee, C.M., Cable, M.L., Hook, S.J., Green, R.O., Ustin, S.L., Mandl, D.J., & Middleton, E.M. (2015). An
712 introduction to the NASA Hyperspectral InfraRed Imager (HyspIRI) mission and preparatory activities.
713 *Remote Sensing of Environment, 167*, 6-19

714 Lewis, S.A., Hudak, A.T., Robichaud, P.R., Morgan, P., Satterberg, K.L., Strand, E.K., Smith, A.M.S.,
715 Zamudio, J.A., & Lentile, L.B. (2017). Indicators of burn severity at extended temporal scales: a decade of
716 ecosystem response in mixed-conifer forests of western Montana. *International Journal of Wildland Fire,*
717 *26*, 755-771

718 Li, W.K., Guo, Q.H., Jakubowski, M.K., & Kelly, M. (2012). A New Method for Segmenting Individual Trees
719 from the Lidar Point Cloud. *Photogrammetric Engineering and Remote Sensing, 78*, 75-84

720 Lippitt, C.D., Rogan, J., Toledano, J., Sangermano, F., Eastman, J.R., Mastro, V., & Sawyer, A. (2008).
721 Incorporating anthropogenic variables into a species distribution model to map gypsy moth risk.
722 *ecological modelling, 210*, 339-350

723 Logan, J.A., Régnière, J., & Powell, J.A. (2003). Assessing the impacts of global warming on forest pest
724 dynamics. *Frontiers in Ecology and the Environment, 1*, 130-137

725 Lu, X., Guo, Q., Li, W., & Flanagan, J. (2014). A bottom-up approach to segment individual deciduous
726 trees using leaf-off lidar point cloud data. *ISPRS Journal of Photogrammetry and Remote Sensing, 94*, 1-
727 12

728 Man, G. (2010). *Major forest insect and disease conditions in the United States: 2009 update*. USDA
729 Forest Service

730 McCarley, T.R., Kolden, C.A., Vaillant, N.M., Hudak, A.T., Smith, A.M., Wing, B.M., Kellogg, B.S., & Kreitler,
731 J. (2017). Multi-temporal LiDAR and Landsat quantification of fire-induced changes to forest structure.
732 *Remote Sensing of Environment, 191*, 419-432

733 McDowell, N.G., Coops, N.C., Beck, P.S.A., Chambers, J.Q., Gangodagamage, C., Hicke, J.A., Huang, C.-y.,
734 Kennedy, R., Krofcheck, D.J., & Litvak, M. (2015). Global satellite monitoring of climate-induced
735 vegetation disturbances. *Trends in plant science, 20*, 114-123

736 Meng, R., Dennison, P., Jamison, L., van Riper, C., Nager, P., Hultine, K., Bean, D., & Dudley, T. (2012).
737 Detection of Tamarisk Defoliation by the Northern Tamarisk Beetle Based on Multitemporal Landsat 5
738 Thematic Mapper Imagery. *GIScience & Remote Sensing, 49*, 510-537

739 Meng, R., & Dennison, P.E. (2015). Spectroscopic analysis of green, desiccated and dead tamarisk
740 canopies. *Photogrammetric Engineering & Remote Sensing, 81*, 199-207

741 Meng, R., Dennison, P.E., Huang, C., Moritz, M.A., & D'Antonio, C. (2015). Effects of fire severity and
742 post-fire climate on short-term vegetation recovery of mixed-conifer and red fir forests in the Sierra
743 Nevada Mountains of California. *Remote Sensing of Environment, 171*, 311-325

744 Meng, R., Wu, J., Schwager, K.L., Zhao, F., Dennison, P.E., Cook, B.D., Brewster, K., Green, T.M., & Serbin,
745 S.P. (2017). Using high spatial resolution satellite imagery to map forest burn severity across spatial
746 scales in a Pine Barrens ecosystem. *Remote Sensing of Environment, 191*, 95-109

747 Meng, R., Wu, J., Zhao, F., Cook, B.D., Hanavan, R.P., & Serbin, S.P. (2018). Measuring short-term post-
748 fire forest recovery across a burn severity gradient in a mixed pine-oak forest using multi-sensor remote
749 sensing techniques. *Remote Sensing of Environment, 210*, 282-296

750 Meng, R., & Zhao, F. (2017). Remote Sensing of Fire Effects: A Review for Recent Advances in Burned
751 Area and Burn Severity Mapping. In G.P. Petropoulos, & T. Islam (Eds.), *Remote Sensing of*
752 *Hydrometeorological Hazards* (pp. 261-281). Boca Raton, FL: CRC Press/ Taylor & Francis Group

753 Millar, C.I., & Stephenson, N.L. (2015). Temperate forest health in an era of emerging megadisturbance.
754 *Science, 349*, 823-826

755 Nagler, P.L., Pearlstein, S., Glenn, E.P., Brown, T.B., Bateman, H.L., Bean, D.W., & Hultine, K.R. (2014).
756 Rapid dispersal of saltcedar (Tamarix spp.) biocontrol beetles (Diorhabda carinulata) on a desert river
757 detected by phenocams, MODIS imagery and ground observations. *Remote Sensing of Environment, 140*,
758 206-219

759 Naidoo, R., & Lechowicz, M.J. (2001). Effects of gypsy moth on radial growth of deciduous trees. *Forest*
760 *Science, 47*, 338-348

761 Olsson, P.-O., Jönsson, A.M., & Eklundh, L. (2012). A new invasive insect in Sweden – Physokermes
762 inopinatus: Tracing forest damage with satellite based remote sensing. *Forest Ecology and Management,*
763 *285*, 29-37

764 Oumar, Z., & Mutanga, O. (2014). Integrating environmental variables and WorldView-2 image data to
765 improve the prediction and mapping of Thaumastocoris peregrinus (bronze bug) damage in plantation
766 forests. *ISPRS Journal of Photogrammetry and Remote Sensing, 87*, 39-46

O'brien, R.M. (2007). A caution regarding rules of thumb for variance inflation factors. *Quality & Quantity, 41*, 673-690

Parkan, M. (2017). Digital Forestry Toolbox. In. http://mparkan.github.io/Digital-Forestry-Toolbox/

Pasquarella, V.J., Bradley, B.A., & Woodcock, C.E. (2017). Near-Real-Time Monitoring of Insect Defoliation Using Landsat Time Series. *Forests, 8*, 275

Quintano, C., Fernández-Manso, A., & Roberts, D.A. (2013). Multiple Endmember Spectral Mixture Analysis (MESMA) to map burn severity levels from Landsat images in Mediterranean countries. *Remote Sensing of Environment, 136*, 76-88

Radeloff, V.C., Mladenoff, D.J., & Boyce, M.S. (1999). Detecting Jack Pine Budworm Defoliation Using Spectral Mixture Analysis: Separating Effects from Determinants. *Remote Sensing of Environment, 69*, 156-169

Reiners, W. (1967). Relationships between vegetational strata in the pine barrens of central Long Island, New York. *Bulletin of the Torrey Botanical Club*, 87-99

Roberts, D.A., Gardner, M., Church, R., Ustin, S., Scheer, G., & Green, R.O. (1998). Mapping Chaparral in the Santa Monica Mountains Using Multiple Endmember Spectral Mixture Models. *Remote Sensing of Environment, 65*, 267-279

Rock, B.N., Hoshizaki, T., & Miller, J.R. (1988). Comparison of in situ and airborne spectral measurements of the blue shift associated with forest decline. *Remote Sensing of Environment, 24*, 109-127

Rullan-Silva, C.D., Olthoff, A.E., de la Mata, J.A.D., & Pajares-Alonso, J.A. (2013). Remote monitoring of forest insect defoliation-A Review. *Forest Systems, 22*, 377-391

Seidl, R., Müller, J., Hothorn, T., Bässler, C., Heurich, M., & Kautz, M. (2016). Small beetle, large‐scale drivers: how regional and landscape factors affect outbreaks of the European spruce bark beetle. *Journal of applied ecology, 53*, 530-540

Seidl, R., Schelhaas, M.-J., Rammer, W., & Verkerk, P.J. (2014). Increasing forest disturbances in Europe and their impact on carbon storage. *Nature climate change, 4*, 806-810

792 Seidl, R., Thom, D., Kautz, M., Martin-Benito, D., Peltoniemi, M., Vacchiano, G., Wild, J., Ascoli, D., Petr,
793 M., & Honkaniemi, J. (2017). Forest disturbances under climate change. *Nature Climate Change, 7*, 395-
794 402

795 Senf, C., Campbell, E.M., Pflugmacher, D., Wulder, M.A., & Hostert, P. (2017a). A multi-scale analysis of
796 western spruce budworm outbreak dynamics. *Landscape Ecology, 32*, 501-514

797 Senf, C., Pflugmacher, D., Heurich, M., & Krueger, T. (2017b). A Bayesian hierarchical model for
798 estimating spatial and temporal variation in vegetation phenology from Landsat time series. *Remote*
799 *sensing of environment, 194*, 155-160

800 Senf, C., Pflugmacher, D., Wulder, M.A., & Hostert, P. (2015). Characterizing spectral–temporal patterns
801 of defoliator and bark beetle disturbances using Landsat time series. *Remote Sensing of Environment,*
802 *170*, 166-177

803 Senf, C., Seidl, R., & Hostert, P. (2017c). Remote sensing of forest insect disturbances: Current state and
804 future directions. *International Journal of Applied Earth Observation and Geoinformation, 60*, 49-60

805 Shendryk, I., Broich, M., Tulbure, M.G., McGrath, A., Keith, D., & Alexandrov, S.V. (2016). Mapping
806 individual tree health using full-waveform airborne laser scans and imaging spectroscopy: A case study
807 for a floodplain eucalypt forest. *Remote Sensing of Environment, 187*, 202-217

808 Solberg, S., Naesset, E., Hanssen, K.H., & Christiansen, E. (2006). Mapping defoliation during a severe
809 insect attack on Scots pine using airborne laser scanning. *Remote Sensing of Environment, 102*, 364-376

810 Somers, B., Verbesselt, J., Ampe, E.M., Sims, N., Verstraeten, W.W., & Coppin, P. (2010). Spectral
811 mixture analysis to monitor defoliation in mixed-aged Eucalyptus globulus Labill plantations in southern
812 Australia using Landsat 5-TM and EO-1 Hyperion data. *International Journal of Applied Earth Observation*
813 *and Geoinformation, 12*, 270-277

814 Spruce, J.P., Sader, S., Ryan, R.E., Smoot, J., Kuper, P., Ross, K., Prados, D., Russell, J., Gasser, G., McKellip,
815 R., & Hargrove, W. (2011). Assessment of MODIS NDVI time series data products for detecting forest
816 defoliation by gypsy moth outbreaks. *Remote Sensing of Environment, 115*, 427-437

Stuffler, T., Kaufmann, C., Hofer, S., Förster, K.P., Schreier, G., Müller, A., Eckardt, A., Bach, H., Penne, B., & Benz, U. (2007). The EnMAP hyperspectral imager—An advanced optical payload for future applications in Earth observation programmes. *Acta Astronautica, 61*, 115-120

Thompson, L.M., Faske, T.M., Banahene, N., Grim, D., Agosta, S.J., Parry, D., Tobin, P.C., Johnson, D.M., & Grayson, K.L. (2017). Variation in growth and developmental responses to supraoptimal temperatures near latitudinal range limits of gypsy moth Lymantria dispar (L.), an expanding invasive species. *Physiological Entomology, 42*, 181-190

Townsend, P.A., Eshleman, K.N., & Welcker, C. (2004). Remote sensing of gypsy moth defoliation to assess variations in stream nitrogen concentrations. *Ecological Applications, 14*, 504-516

Townsend, P.A., Singh, A., Foster, J.R., Rehberg, N.J., Kingdon, C.C., Eshleman, K.N., & Seagle, S.W. (2012). A general Landsat model to predict canopy defoliation in broadleaf deciduous forests. *Remote Sensing of Environment, 119*, 255-265

Trumbore, S., Brando, P., & Hartmann, H. (2015). Forest health and global change. *Science, 349*, 814-818

Warner, T.A., Skowronski, N.S., & Gallagher, M.R. (2017). High spatial resolution burn severity mapping of the New Jersey Pine Barrens with WorldView-3 near-infrared and shortwave infrared imagery. *International Journal of Remote Sensing, 38*, 598-616

White, J.C., Coops, N.C., Wulder, M.A., Vastaranta, M., Hilker, T., & Tompalski, P. (2016). Remote sensing technologies for enhancing forest inventories: A review. *Canadian Journal of Remote Sensing, 42*, 619-641

White, J.C., Wulder, M.A., Brooks, D., Reich, R., & Wheate, R.D. (2005). Detection of red attack stage mountain pine beetle infestation with high spatial resolution satellite imagery. *Remote Sensing of Environment, 96*, 340-351

Wulder, M.A., White, J.C., Coops, N.C., & Butson, C.R. (2008). Multi-temporal analysis of high spatial resolution imagery for disturbance monitoring. *Remote Sensing of Environment, 112*, 2729-2740

Yamashita, T., Yamashita, K., & Kamimura, R. (2007). A stepwise AIC method for variable selection in linear regression. *Communications in Statistics—Theory and Methods, 36*, 2395-2403

Zarco-Tejada, P.J., Hornero, A., Hernández-Clemente, R., & Beck, P.S.A. (2018). Understanding the temporal dimension of the red-edge spectral region for forest decline detection using high-resolution hyperspectral and Sentinel-2a imagery. *ISPRS Journal of Photogrammetry and Remote Sensing, 137*, 134-148

Zhao, F., Huang, C., & Zhu, Z. (2015). Use of vegetation change tracker and support vector machine to map disturbance types in greater yellowstone ecosystems in a 1984–2010 Landsat time series. *IEEE Geoscience and Remote Sensing Letters, 12*, 1650-1654

List of figure captions

Figure 1. Crown-scale defoliation survey transects within the study area (the background imagery is the true color RGB composition (657 nm (red), 564 nm (green), and 484 nm (blue)) derived from NASA Goddard's LiDAR, Hyperspectral and Thermal (G-LiHT) measurements acquired on June 14, 2016); in-situ pictures showing crown-scale defoliation severity scores (i.e., percentage of leaf area remaining). (For interpretation of the references to color in this figure legend, the reader is referred to the web version of this article.)

Figure 2. Workflow in this study for mapping canopy defoliation by herbivorous insects at the individual tree level

Figure 3. Green vegetation (GV) (a) and non-photosynthetic vegetation (NPV) (b) endmembers selected for use with MESMA. (For interpretation of the references to color in this figure legend, the reader is referred to the web version of this article.)

Figure 4. Mean crown-scale spectra and their 95% confidence interval for the following defoliation severity (i.e., percentage of leaf area remaining) groups extracted from the 2016 G-LiHT imaging spectroscopy measurement: 0-20% leaf area remaining; 20-40% leaf area remaining; 40-60% leaf area remaining; 60-80% leaf area remaining; 80-100% leaf area

remaining; To avoid noise, percentage of leaf area remaining was grouped into 20% intervals, consistent with previous similar remote sensing studies (Townsend et al. 2012). (For interpretation of the references to color in this figure legend, the reader is referred to the web version of this article.)

Figure 5. Change in canopy height profile within five defoliation severity (i.e., percentage of leaf area remaining) groups from 2015 to 2016 calculated from the G-LiHT LiDAR measurements; negative values indicate the decrease in vertical laser return point distributions from 2015 to 2016 at certain height interval, and positive values indicate the opposite trend; bars show the standard errors for each defoliation severity group. To avoid noise, percentage of leaf area remaining was grouped into 20% intervals, consistent with previous similar remote sensing studies (Townsend et al. 2012). (For interpretation of the references to color in this figure legend, the reader is referred to the web version of this article.)

Figure 6. Scatter plot matrix of percentage of leaf area remaining vs. 2016 IS and LiDAR metrics used for model training: a. MESMA NPV fraction; b. MESMA oak fraction; c. MESMA understory fraction; d. LiDAR skewness; e. LiDAR Intensity kurtosis; f. LiDAR Intensity skewness; g. 20th bincentile height; h. 30th bincentile height; i. 40th bincentile height; j. 50th bincentile height; k. 60th bincentile height; l. 70th bincentile height; m.80th bincentile height; n. 90th bincentile height.

Figure 7. Boxplots of adjusted R-squared (a) and RMSE (b) values using IS-only predictor variables, LiDAR-only predictor variables and their combination for predicting canopy defoliation of validation datasets. p values show the least significance of paired Wilcoxon signed rank test results.

Figure 8. Average and standard error values of MESMA fractions at five leaf area remaining (i.e., canopy defoliation severity) groups for 2015 and 2016: a. GV-oak fraction; b. GV-understory fraction; c. NPV fraction. (For interpretation of the references to color in this figure legend, the reader is referred to the web version of this article.)

Figure 9. Average and standard error values of LiDAR predictors selected by stepwise AIC-based method (see Section 4.4) for mapping crown-scale canopy defoliation at five leaf area remaining (i.e., canopy defoliation severity) groups for 2015 and 2016: a. B70; b. Intensity skewness; c. Kurtosis.(For interpretation of the references to color in this figure legend, the reader is referred to the web version of this article.)

Figure 10. Crown-scale percentage of oak leaf area remaining (i.e., oak canopy defoliation severity) map at 1m resolution in a mixed pine-oak forest, Long island, NY in 2016; the inset subplots show a partial zoom-in view of the defoliation severity map and corresponding MESMA oak fraction (a) and LiDAR-derived B70 (i.e., 70th bincentile height) (b). The rectangle on the oak canopy defoliation severity map shows the inset extent. (For interpretation of the references to color in this figure legend, the reader is referred to the web version of this article.)

List of figure and table captions of supplementary materials

Figure S1. Frequency distributions of adjusted R-squared (a) and RMSE (b) values using IS-only predictor variables, LiDAR-only predictor variables and their combination for predicting canopy defoliation of validation datasets.

Table S1. Confusion matrix of tree canopy classification in 2012

908 **Table S2.** G-LiHT imaging spectroscopy derived visible-near-infrared spectral indices and their

909 linear correlations with percentage leaf area remaining (i.e., defoliation severity) of surveyed oak